Post-Print

This is the accepted version of:

The final publication is available at https://doi.org/10.1016/j.mechmachtheory.2020.104181

Access to the published version may require subscription.

When citing this work, cite the original published paper.

Permanent link to this version
http://hdl.handle.net/11311/1153688

A tight coupling scheme for smooth/non-smooth multibody co-simulation of a particle damper

Runsen Zhang[a,b,*], Huimin Zhang[a,b], Andrea Zanoni[b], Qi Wang[a], Pierangelo Masarati[b]

[a]*School of Aeronautic Science and Engineering, Beihang University, Beijing 100083, China*
[b]*Dipartimento di Scienze e Tecnologie Aerospaziali, Politecnico di Milano, Milano 20156, Italy*

Abstract

To simulate coupled problems, composed of smooth and non-smooth particle subsystems, a tight, i.e. iterative coupling scheme is implemented. In the proposed setup, the non-smooth solver iterations are enclosed in each iteration of the smooth solver at every time step. The stability properties of the coupling scheme are tested using Dahlquist's test equations for co-simulation methods, highlighting the higher degree of stability of the tight coupling scheme, compared to the loose, non-iterative one. Results also denote that the properties of the solvers used to analyse the subsystems play an important role in the stability of co-simulation. The performance of the proposed scheme is further assessed by two illustrative examples: a particle damper subjected to prescribed motion, and a cantilever beam, modelled using finite elements, with a particle damper mounted at the free end. The proposed numerical solutions agree well with results from reduced order models and experiments, which demonstrates that the proposed scheme can effectively handle coupled problems of multibody systems and particle dampers.

Keywords: Co-simulation methods, Particle dampers, Stability analysis, Non-smooth dynamics

1. INTRODUCTION

Particle dampers, consisting of particles in a cavity or container, are widely-used passive vibration suppression devices in engineering [1, 2]. Unlike traditional viscous dampers, particle dampers dissipate energy and transfer momentum through the non-smooth interaction among particles and walls [3], so they can be effective even in some harsh environments [4, 5]. However, due to the frictional contacts among particles, modeling and theoretically studying particle dampers is still a challenging problem, and much research focuses on numerical simulation [6, 7, 8]. The most popular numerical method in the study of particle dampers is the Discrete Element Method (DEM) [9]. It models particles as spheres with local deformation, and describes

---

*Corresponding author.
Email addresses:* `buaa_zhangrunsen@163.com` (Runsen Zhang), `huimin0327@163.com` (Huimin Zhang), `andrea.zanoni@polimi.it` (Andrea Zanoni), `bhwangqi@sina.com` (Qi Wang), `pierangelo.masarati@polimi.it` (Pierangelo Masarati)

contacts by the Hertz model or some modified Hertz models [10], where the contact force is a function of the penetration depth and velocity [11, 12].

Another method, based on the non-smooth dynamics theory, is also available for simulating interactions in rigid bodies through frictional contacts [13, 14]. According to this method, the equations of motion are expressed as measure differential equations, along with complementarity conditions that describe frictional contacts [14]. After time discretization, the equations are transformed into equivalent linear/nonlinear complementarity problems (L/NCPs) [13, 14], which can be solved using optimization methods [15, 16]. Such non-smooth method is commonly used in mechanical systems with unilateral constraints [17] or imperfect joints [18], where yet the number of frictional contacts is limited. For dense granular flows with a large number of frictional contacts, Tasora and Anitescu [19] proposed a novel non-smooth solver based on cone complementarity problems (CCPs), and released their method in the open-source library Chrono::Engine as a general method for coupled smooth/non-smooth systems. The solver can monolithically solve complete multibody-particles coupled systems [19, 20, 21], but the only available integrator in the method is the semi-implicit Euler scheme. If higher-order accuracy or tunable algorithmic dissipation is needed, an implicit non-smooth scheme may be preferable [21]. For this purpose, several non-smooth implicit methods that can provide tunable algorithm dissipation, such as the non-smooth generalized-α method [22], and the mixed non-smooth time-stepping schemes [23], were developed. The authors of the present work also improved the implicit integration methods to avoid accuracy loss induced by friction [24], and developed a framework of implicit integration for mechanical systems with frictional contacts [25]. However, these non-smooth implicit methods have been only applied to problems with a limited number of contacts so far.

To investigate the interaction of mechanical systems with particle dampers, a common way is to reduce the primary system to an equivalent single degree-of-freedom (DoF) system and to model the particle damper using the DEM [6, 7, 26]. This approach cannot account for the complex motion of multi-DoF primary systems. For the latter case, Lu et al. [27] developed a modified numerical method based on the DEM, where the dynamics equations of the primary system, subjected to the contact forces resulting from the particle damper, are expressed as ordinary differential equations. Their method was applied to simulate multi-story buildings with particle dampers [3]. For general mechanical systems, usually modelled as multibody systems with kinematic constraints, the dynamics equations are described as differential algebraic equations (DAEs) [28] using the multibody dynamics (MBD) approach. However, since neither MBD nor DEM alone can effectively handle the coupled system, the primary system and the particle damper are often treated separately by means of co-simulation. In this case, different solvers, executed in parallel [29] or in series [30], exchange information with each other at discrete times [31] to obtain the coupled dynamical responses.

To solve the coupled granular-multibody system, most studies use loose coupling schemes, also called explicit coupling schemes or non-iterative coupling schemes [32]. Among them, a two-way loose coupling method is commonly used, by which different solvers adopt individual time steps, with the synchronization at a macro time step. One such loose co-simulation scheme between MSC/ADAMS$^{\circledR}$, a commercial software for MBD, and EDEM$^{\circledR}$, a DEM tool, was tailored in [33], where the stability of the co-simulation is numerically assessed by several simple systems with particle dampers, which shows that a small communication interval is necessary to obtain algorithmically stable results. Using different MBD and DEM tools, loose coupling schemes for coupled dynamics of multibody systems with particles were also obtained in [8, 34]. Apart from the co-simulation between MBD tools and DEM tools, a loose co-simulation

2

framework between the MBD method and the non-smooth method was proposed in [35] and implemented in the open-source code, Chrono::Engine. Different modules in the codes cooperate with each other in parallel, to efficiently study a vehicle-terrain interaction problem. However, for such loose/explicit co-simulation schemes, since only limited information is exchanged at a discrete time, in some cases stable results cannot be easily obtained.

To study the stability of co-simulation methods, Kübler et al. [36] proposed the concept of zero-stability, and proved that a loose co-simulation method is stable if there is no algebraic loop among subsystems. For coupled systems with algebraic loops, they presented two tight coupling schemes, with iterations of the coupling equations and with iterations of the global integration step, to guarantee the zero-stability [37]. A semi-implicit co-simulation scheme consisting of two steps was proposed in [38], which first predicts the state variables, and then corrects the integration using a Jacobian matrix. Using Dahlquist's test equations for co-simulation methods, the stability properties of the semi-implicit scheme were discussed, finding that this semi-implicit scheme performs better than the explicit coupling scheme without the correction step [38, 39]. In the above mentioned implicit/semi-implicit schemes, the sub-solvers are characterized as simulation blocks with inputs and outputs, and all integrators need to be reinitialized and repeated at each time step. Peiret et al. [31] proposed reduced interface models (RIMs) for multi-physics systems, and applied RIMs to the loose co-simulation scheme of non-smooth multibody systems with hydraulic components [40]. Using RIMs, the influence of the extrapolation methods and integrators in each subsystem were also studied for two mechanical-hydraulic systems, which indicates that the accuracy of the co-simulation can be improved by an appropriate selection of the integration schemes [41]. The above mentioned techniques can all improve the stability of the co-simulation, but little attention has been paid so far to the co-simulation between a MBD solver and a DEM solver or a non-smooth solver.

This paper aims at developing a stable co-simulation framework based on MBD and the non-smooth method, to study coupled systems composed of smooth multibody systems and non-smooth particle dampers. As opposed to the loose co-simulation framework used before [33, 34, 35], a tight coupling scheme with iterative refinement process is established in the present work. In the tight coupling scheme, the non-smooth solver is embedded into the iteration process of the MBD solver, so the iterative process of the MBD solver can be employed and only the non-smooth solver's step needs to be repeated during each iteration. The stability properties of the coupling scheme are studied using Dahlquist's test equations for co-simulation methods, which are interpreted as the equations governing the dynamics of a linear two-mass oscillator system, from the mechanical point of view [39]. The influence of the two solvers on the stability properties is discussed for different system parameters. The coupling scheme is subsequently evaluated using the experiment in [26], which consists of a particle damper subjected to prescribed motion. Good agreement of the numerical solution obtained using the proposed scheme, with that resulting from the monolithic method, and with experimental results [26], can be observed. Finally, a detailed finite-volume model of a cantilever beam carrying a particle damper at the free end is simulated using the proposed scheme. The results corresponding to the first natural frequency are verified using a reduced model; the dynamic response in the proximity of higher-order natural frequencies and under centrifugal loads can also be simulated by the proposed scheme and model, which shows the dissipation of the particle damper in various cases.

This paper is organized as follows. In Section 2, the coupled system consisting of the multibody system and the particle damper is decomposed using the force/displacement technique. Their equations are established using the MBD and the non-smooth method, respectively. Section 3 provides the proposed tight coupling scheme, and discusses relevant aspects of the imple-
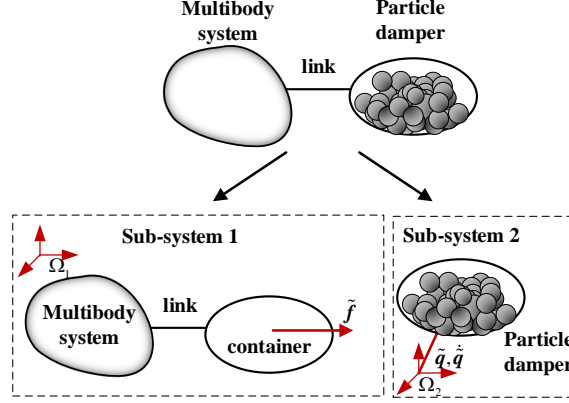
3

Figure 1: Force/displacement decomposition of the coupled system.

mentation of the co-simulation. The stability properties of the coupling scheme are discussed using the two-mass oscillator in Section 4. In Section 5, two coupled systems, the one in the experiment [26] and a cantilever beam carrying a particle damper at the free end, are co-simulated using the proposed coupling scheme. Finally, conclusions are drawn in Section 6.

2. FORMULATION

A multibody system connected to a particle damper is decomposed into two subsystems, as shown in Fig. 1, according to the force/displacement decomposition technique [29]. Subsystem 1 contains the multibody system and the container of the particle damper, which is excited by the forces and torques from the particles, denoted as $\tilde{\mathbf{f}}$. Subsystem 2 includes the particle damper, where the motion of its container, $\tilde{\mathbf{q}}$ and $\dot{\tilde{\mathbf{q}}}$, is obtained from subsystem 1. After the decomposition, different solvers can be employed to deal with each subsystem. They communicate with each other by respectively exchanging the dynamic data $\tilde{\mathbf{f}}$, and the kinematic data $\tilde{\mathbf{q}}$ and $\dot{\tilde{\mathbf{q}}}$.

2.1. Formulation for multibody systems

The dynamic equation of a general multibody system with constraints is formulated as a set of DAEs by MBD [28]

$$
\begin{cases}
\mathbf{M}\ddot{\mathbf{q}} + \boldsymbol{\phi}_{\mathbf{q}}^{\mathrm{T}}\boldsymbol{\lambda}_{\phi} + \boldsymbol{\psi}_{\dot{\mathbf{q}}}^{\mathrm{T}}\boldsymbol{\lambda}_{\psi} - \mathbf{f} = \mathbf{0}, \\
\boldsymbol{\phi}(\mathbf{q}, t) = \mathbf{0}, \\
\boldsymbol{\psi}(\mathbf{q}, \dot{\mathbf{q}}, t) = \mathbf{0},
\end{cases}
\tag{1}
$$

where

    · $\mathbf{M}$ is the mass matrix;

    · $\mathbf{q}$ is the system's generalized coordinates vector (the dot denotes the total derivative with respect to time t);

    · $\boldsymbol{\phi} = \mathbf{0}$ and $\boldsymbol{\psi} = \mathbf{0}$ are the holonomic and non-holonomic constraint equations vectors; the corresponding Lagrangian multipliers vectors are $\boldsymbol{\lambda}_{\phi}$ and $\boldsymbol{\lambda}_{\psi}$, respectively;

4

- $\mathbf{f}$ is the generalized force vector, including the input coupling variable $\tilde{\mathbf{f}}$ resulting from the particles;

- the operator $(\cdot)_{\mathbf{q}}$ denotes the partial derivative matrix with respect to vector $\mathbf{q}$.

To solve Eq. (1), the A/L stable implicit linear two-step scheme presented in [28] is employed,

$$\mathbf{y}_n = \sum_{i=1,2} a_i \mathbf{y}_{n-i} + h \sum_{i=0,1,2} b_i \dot{\mathbf{y}}_{n-i}, \tag{2}$$

where

- h is the time step size, and the subscript $n \in \mathbb{N}$ indicates the integration step at time $t = t_n$;

- $\mathbf{y} = [\mathbf{q}; \dot{\mathbf{q}}; \lambda_\phi; \lambda_\psi]$ is the state vector;

- a_i and b_i are the parameters of the integrator, defined as [28]:

$$\begin{array}{ll} & b_0 = \delta + 1/2, \\ a_1 = 1 - \beta, & b_1 = \beta/2 + 1/2 - 2\delta, \\ a_2 = \beta, & b_2 = \beta/2 + \delta, \end{array} \tag{3}$$

with

$$\begin{cases} \beta = \dfrac{3(1 - |\rho_\infty|)^2 + 4(2|\rho_\infty| - 1)}{4 - (1 - |\rho_\infty|)^2}, \\[3mm] \delta = \dfrac{(1 - |\rho_\infty|)^2}{2\left(4 - (1 - |\rho_\infty|)^2\right)}, \end{cases} \tag{4}$$

where $\rho_\infty \in [0, 1]$ denotes the asymptotic spectral radius of the scheme. It denotes the degree of algorithmic dissipation; a smaller ρ_∞ means stronger algorithmic dissipation. For general purpose applications, involving lightly damped structures, $\rho_\infty = 0.6$ is recommended as a good trade-off between accuracy and algorithmic dissipation [28].

This integrator is second-order accurate and A-stable (unconditionally stable) with the given parameters, as shown in Eq. (3). It offers tunable algorithmic dissipation by adjusting ρ_∞, and becomes L-stable (with the maximum degree of algorithmic dissipation) when $\rho_\infty = 0$ [28]. Combined with the discrete DAEs at t_{n+1}, the integration scheme can give the numerical results of $\mathbf{y}_{n+1}$ and $\dot{\mathbf{y}}_{n+1}$. At each step, a nonlinear solver, such as the Newton-Raphson iteration, is also required to solve the implicit equations of DAEs, and to start the iteration, $\dot{\mathbf{y}}_{n+1}^{(0)}$ is predicted by the cubic Hermitian extrapolation

$$\dot{\mathbf{y}}_{n+1}^{(0)} = -\frac{12}{h}(\mathbf{y}_n - \mathbf{y}_{n-1}) + 8\dot{\mathbf{y}}_n + 5\dot{\mathbf{y}}_{n-1}, \tag{5}$$

$\mathbf{y}_{n+1}^{(0)}$ is obtained by substituting Eq. (5) into the integration scheme (2), as

$$\mathbf{y}_{n+1}^{(0)} = \sum_{i=1,2} a_i \mathbf{y}_{n+1-i} + h \sum_{i=1,2} b_i \dot{\mathbf{y}}_{n+1-i} + h b_0 \left[-\frac{12}{h}(\mathbf{y}_n - \mathbf{y}_{n-1}) + 8\dot{\mathbf{y}}_n + 5\dot{\mathbf{y}}_{n-1} \right]. \tag{6}$$

The solution procedure has been embedded into the free, general-purpose multibody dynamics solver MBDyn[1], which in the present work is adopted for subsystem 1.

---

[1] http://www.mbdyn.org/, last accessed June 2020.

2.2. Non-smooth method

The non-smooth method is based on the assumption that particles are rigid, which is appropriate for very stiff particles, such as sand or steel balls, for instance [19]. This method has been widely used for granular systems, where a large number of particles are efficiently simulated [19, 20, 35], and is employed for the particle damper in subsystem 2, where it is reasonable to assume particles as rigid balls when they are stiff enough. With the assumption of rigid particles, the frictional contacts among particles are expressed as frictional unilateral constraints. Friction forces and contact forces are given based on the Coulomb friction model and the Signorini condition [14, 42].

2.2.1. System description

According to the non-smooth theory, the particle damper, consisting of a rigid container and N_b particles, is formulated as $(N_b + 1)$ rigid bodies. The corresponding generalized coordinates and velocities are defined as

$$
\begin{cases}
\mathbf{x}_P = \begin{bmatrix} \mathbf{r}_0^{\mathrm{T}} & \boldsymbol{\varepsilon}_0^{\mathrm{T}} & \mathbf{r}_1^{\mathrm{T}} & \boldsymbol{\varepsilon}_1^{\mathrm{T}} & \dots & \mathbf{r}_{N_b}^{\mathrm{T}} & \boldsymbol{\varepsilon}_{N_b}^{\mathrm{T}} \end{bmatrix}^{\mathrm{T}} \in \mathbb{R}^{7(N_b+1)}, \\
\dot{\mathbf{x}}_P = \begin{bmatrix} \dot{\mathbf{r}}_0^{\mathrm{T}} & \dot{\boldsymbol{\varepsilon}}_0^{\mathrm{T}} & \dot{\mathbf{r}}_1^{\mathrm{T}} & \dot{\boldsymbol{\varepsilon}}_1^{\mathrm{T}} & \dots & \dot{\mathbf{r}}_{N_b}^{\mathrm{T}} & \dot{\boldsymbol{\varepsilon}}_{N_b}^{\mathrm{T}} \end{bmatrix}^{\mathrm{T}} \in \mathbb{R}^{7(N_b+1)},
\end{cases}
\tag{7}
$$

where $\mathbf{r}_j$ and $\boldsymbol{\varepsilon}_j$ ($j = 0, 1, 2, ..., N_b$) denote the displacements of the center of mass, and the Euler's quaternion, of body j, respectively. Optionally, $\dot{\boldsymbol{\varepsilon}}_j$ can be replaced by the angular velocity in the local coordinate $\bar{\omega}_j$; the generalized velocity can thus be rewritten as

$$
\mathbf{v}_P = \begin{bmatrix} \dot{\mathbf{r}}_0^{\mathrm{T}} & \bar{\omega}_0^{\mathrm{T}} & \dot{\mathbf{r}}_1^{\mathrm{T}} & \bar{\omega}_1^{\mathrm{T}} & \dots & \dot{\mathbf{r}}_{N_b}^{\mathrm{T}} & \bar{\omega}_N^{\mathrm{T}} \end{bmatrix}^{\mathrm{T}} \in \mathbb{R}^{6(N_b+1)},
\tag{8}
$$

The two expressions are related by a transformation $\dot{\mathbf{x}}_P = L(\mathbf{x}_P)\mathbf{v}_P$.

2.2.2. Signorini condition and Coulomb's friction law

For the contact i between any two rigid bodies A and B, as shown in Fig. 2, the non-penetration condition is defined by the unilateral constraint, $\Phi_i \geq 0$. When A and B are in contact, namely $\Phi_i = 0$, the normal contact force generated from the contact is expressed as

$$
\mathbf{F}_{N_i} = \hat{\gamma}_{\mathbf{n}_i} \cdot \mathbf{n}_i \geq 0,
\tag{9}
$$

where $\mathbf{n}_i$ represents the normal vector at the contact point, and $\hat{\gamma}_{\mathbf{n}_i}$ is the magnitude of the contact force. When the contact is inactive, $\Phi_i > 0$, the normal contact force $\mathbf{F}_{N_i}$ vanishes. This set of relationships between Φ_i and $\mathbf{F}_{N_i}$ is described by the complementarity theory, i.e. the Signorini condition [14]

$$
0 \leq \hat{\gamma}_{\mathbf{n}_i} \quad \perp \quad \Phi_i \geq 0.
\tag{10}
$$

The Signorini condition needs to be expressed at the velocity level, when the equations of motion are formulated at the impulse level [20], i.e. the velocity Signorini condition [14]

$$
0 \leq \gamma_{\mathbf{n}_i} \quad \perp \quad v_{\mathbf{n}_i} \geq 0,
\tag{11}
$$

where $\gamma_{\mathbf{n}_i} = h \cdot \hat{\gamma}_{\mathbf{n}_i}$ is the impulse generated by the contact force, and $v_{\mathbf{n}_i}$ is the normal velocity magnitude at the contact point.

The friction force vector of contact i is described as

$$
\hat{\mathbf{F}}_{T_i} = \hat{\gamma}_{\mathbf{u}_i} \mathbf{u}_i + \hat{\gamma}_{\mathbf{w}_i} \mathbf{w}_i,
\tag{12}
$$

where $\mathbf{u}_i$ and $\mathbf{w}_i$ are orthogonal unit vectors defined in the tangent plane, shown in Fig. 2, and $\hat{\gamma}_{\mathbf{u}_i}$ and $\hat{\gamma}_{\mathbf{w}_i}$ are the corresponding coordinates along $\mathbf{u}_i$ and $\mathbf{w}_i$. The friction force vector $\hat{\mathbf{F}}_{T_i}$ is modeled by the Coulomb friction law with equal dynamical and static friction coefficient μ_i. This means that when the relative tangential velocity $\mathbf{v}_{T_i}$ is non-zero, the friction force acts in a direction opposite to $\mathbf{v}_{T_i}$ with magnitude $\mu_i\hat{\gamma}_{\mathbf{n}_i}$, and when $\mathbf{v}_{T_i}$ is zero, the modulus of the friction force is not greater than $\mu_i\hat{\gamma}_{\mathbf{n}_i}$. The relationship between $\hat{\mathbf{F}}_{T_i}$ and $\mathbf{v}_{T_i}$ can be expressed using the maximum dissipation principle [20], as

$$(\hat{\gamma}_{\mathbf{u}_i}, \hat{\gamma}_{\mathbf{w}_i}) = \underset{\|\hat{\gamma}_{\mathbf{u}_i}\mathbf{u}_i + \hat{\gamma}_{\mathbf{w}_i}\mathbf{w}_i\| \leq \mu_i\hat{\gamma}_{\mathbf{n}_i}}{\arg\min} \mathbf{v}_{T_i}^{\mathrm{T}} \left(\hat{\gamma}_{\mathbf{u}_i}\mathbf{u}_i + \hat{\gamma}_{\mathbf{w}_i}\mathbf{w}_i\right). \tag{13}$$

At the impulse-velocity level, it can be expressed as

$$(\gamma_{\mathbf{u}_i}, \gamma_{\mathbf{w}_i}) = \underset{\|\gamma_{\mathbf{u}_i}\mathbf{u}_i + \gamma_{\mathbf{w}_i}\mathbf{w}_i\| \leq \mu_i\gamma_{\mathbf{n}_i}}{\arg\min} \mathbf{v}_{T_i}^{\mathrm{T}} \left(\gamma_{\mathbf{u}_i}\mathbf{u}_i + \gamma_{\mathbf{w}_i}\mathbf{w}_i\right), \tag{14}$$

where $\gamma_{\mathbf{u}_i} = h \cdot \hat{\gamma}_{\mathbf{u}_i}$ and $\gamma_{\mathbf{w}_i} = h \cdot \hat{\gamma}_{\mathbf{w}_i}$ represent the frictional impulse components along directions $\mathbf{u}_i$ and $\mathbf{w}_i$.
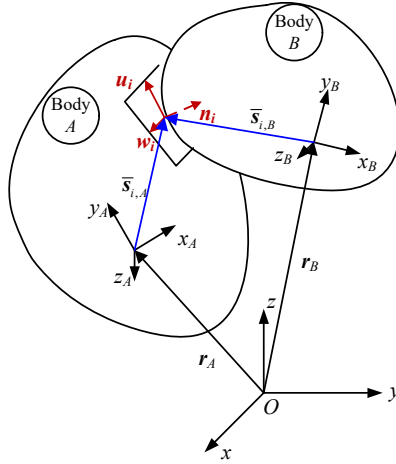

Figure 2: Contact i between two rigid bodies A and B.

2.2.3. Equations of motion

Based on the non-smooth method, the dynamics equations of the particle damper are formulated as differential variational inequalities [19]

$$\begin{cases} \dot{\mathbf{x}}_P = L(\mathbf{x}_P)\mathbf{v}_P, \\ \mathbf{M}_P\dot{\mathbf{v}}_P = \mathbf{f}_P(\mathbf{x}_P, \mathbf{v}_P, t) + \mathbf{G}_{\mathbf{v}_P}^T\hat{\lambda}_{\mathbf{G}} + \sum_{i \in \Pi(\mathbf{x}_P, \delta)} \mathbf{D}_i\hat{\gamma}_i, \\ \mathbf{G}(\mathbf{x}_P, \tilde{\mathbf{q}}, t) = \mathbf{0}, \\ i \in \Pi(\mathbf{x}_P, \delta) : 0 \leq \gamma_{\mathbf{n}_i} \perp v_{\mathbf{n}_i} \geq 0, \\ (\gamma_{\mathbf{u}_i}, \gamma_{\mathbf{w}_i}) = \underset{\|\gamma_{\mathbf{u}_i}\mathbf{u}_i + \gamma_{\mathbf{w}_i}\mathbf{w}_i\| \leq \mu_i\gamma_{\mathbf{n}_i}}{\arg\min} \mathbf{v}_{T_i}^{\mathrm{T}} \left(\gamma_{\mathbf{u}_i}\mathbf{u}_i + \gamma_{\mathbf{w}_i}\mathbf{w}_i\right) \end{cases} \tag{15}$$

where

192 · $\mathbf{M}_P$ is the mass matrix, and $\mathbf{f}_P$ is the generalized force vector, yet not including the reaction
193   forces of unilateral/bilateral constraints;

194 · $\mathbf{G}(\mathbf{x}_P, \tilde{\mathbf{q}}, t) = \mathbf{0}$ denotes the bilateral constraints in this subsystem, and $\hat{\boldsymbol{\lambda}}_{\mathbf{G}}$ is the corre-
195   sponding Lagrangian multipliers vector. The constraint that prescribes the motion of the
196   container according to the value of the input variable $\tilde{\mathbf{q}}$ is included in $\mathbf{G}$. The derivative of
197   the constraint equation with respect to t is

$$\dot{\mathbf{G}}\left(\mathbf{x}_P, \mathbf{v}_P, \tilde{\mathbf{q}}, \dot{\tilde{\mathbf{q}}}, t\right) \equiv \mathbf{G}_{\mathbf{x}_P}\mathbf{v}_P + \mathbf{G}_t + \mathbf{G}_{\tilde{\mathbf{q}}}\dot{\tilde{\mathbf{q}}}, \tag{16}$$

198   where

$$\begin{cases} \mathbf{G}_{\mathbf{x}_P} = \dfrac{\partial \mathbf{G}}{\partial \mathbf{x}_P} \cdot L(\mathbf{x}_P), \\[2mm] \mathbf{G}_t = \dfrac{\partial \mathbf{G}}{\partial t}, \\[2mm] \mathbf{G}_{\tilde{\mathbf{q}}} = \dfrac{\partial \mathbf{G}}{\partial \tilde{\mathbf{q}}}; \end{cases} \tag{17}$$

199 · $\mathbf{D}_i$ is a coefficient matrix related to the vector $\mathbf{x}_P$, representing the generalized normal and
200   tangential directions [17], and $\hat{\boldsymbol{\gamma}}_i = [\hat{\gamma}_{\mathbf{n}_i}, \hat{\gamma}_{\mathbf{u}_i}, \hat{\gamma}_{\mathbf{w}_i}]^{\mathrm{T}}$;

201 · $\Pi(\mathbf{x_P}, \delta) \equiv \{i|\Phi_i \le \delta\}$ (δ is a small quantity) is the index set of all contact points at the
202   current configuration;

203 To avoid drift, the constraint stabilization method proposed in [19] is employed, which reformu-
204 lates the bilateral constraint in Eq. (15) as

$$\frac{\mathbf{G}(\mathbf{x}_P, \tilde{\mathbf{q}}, t)}{h} + \dot{\mathbf{G}}\left(\mathbf{x}_P, \mathbf{v}_P, \tilde{\mathbf{q}}, \dot{\tilde{\mathbf{q}}}, t\right) = 0. \tag{18}$$

205 The semi-implicit Euler scheme at the impulse-velocity level is used to solve the dynamic equa-
206 tion in (15), as [19, 20, 42]

$$\begin{cases} \mathbf{x}_{P,n+1} = \mathbf{x}_{P,n} + h \cdot \mathbf{L}_n\mathbf{v}_{P,n+1}, \\[1mm] \mathbf{M}_P\left(\mathbf{v}_{P,n+1} - \mathbf{v}_{P,n}\right) = h\mathbf{f}_P + \mathbf{G}_{\mathbf{v}_P,n}^{\mathrm{T}}\lambda_{\mathbf{G},n+1} + \sum\limits_{i\in\Pi_n} \mathbf{D}_{i,n}\boldsymbol{\gamma}_{i,n+1}, \\[2mm] \dfrac{\mathbf{G}_n}{h} + \mathbf{G}_{\mathbf{x}_P,n}\mathbf{v}_{P,n+1} + \mathbf{G}_{t,n} + \mathbf{G}_{\tilde{\mathbf{q}},n}\dot{\tilde{\mathbf{q}}}_{\mathbf{n+1}} = 0, \\[2mm] i \in \Pi_n : 0 \le \gamma_{\mathbf{n}_i,n+1} \quad \perp \quad \left(\dfrac{\Phi_{i,n}}{h} + v_{\mathbf{n}_i,n+1} - \mu_i\|\mathbf{v}_{T_i,n+1}\|\right) \ge 0, \\[2mm] (\gamma_{\mathbf{u}_i,n+1}, \gamma_{\mathbf{w}_i,n+1}) = \underset{\|\gamma_{\mathbf{u}_i}\mathbf{u}_i+\gamma_{\mathbf{w}_i}\mathbf{w}_i\|\le\mu_i\gamma_{\mathbf{n}_i}}{\arg\min} \mathbf{v}_{T_i,n+1}^{\mathrm{T}} \left(\gamma_{\mathbf{u}_i,n+1}\mathbf{u}_{i,n+1} + \gamma_{\mathbf{w}_i,n+1}\mathbf{w}_{i,n+1}\right), \end{cases} \tag{19}$$

207 where

208 · $\boldsymbol{\gamma}_i = [\gamma_{\mathbf{n}_i}, \gamma_{\mathbf{u}_i}, \gamma_{\mathbf{w}_i}]^{\mathrm{T}} = h\,[\hat{\gamma}_{\mathbf{n}_i}, \hat{\gamma}_{\mathbf{u}_i}, \hat{\gamma}_{\mathbf{w}_i}]^{\mathrm{T}}$ represents the impulse vector corresponding to the
209   contact force vector;

210 · For constraint stabilization, $\mathbf{v}_{\mathbf{n}_i,n+1} \ge 0$ is replaced by an approximate formula $\dfrac{\Phi_{i,n}}{h} +$
211     $v_{\mathbf{n}_i,n+1} \ge 0$ [14], and a relaxation item $-\mu_i\|\mathbf{v}_{T_i,n+1}\|$ is added to transform Eq. (19) into a
212   cone complementarity problem (CCP) [19, 43].

8

Then, the discrete equations with bilateral constraints and unilateral constraints in Eq. (19) can be solved as a whole by cone optimization methods [16]. The above non-smooth solution method is implemented in the free software library Chrono::Engine[2], which in the present work is utilized to deal with subsystem 2.

It is worth mentioning here that this non-smooth solver can monolithically solve the complete non-smooth multibody system alone [19, 20, 21], but if higher-order accuracy or adjustable algorithmic dissipation is requested for solving the flexible multibody system, the multi-step implicit scheme in Eq. (2) may be preferable. Therefore, the coupling scheme using the smooth/non-smooth solvers MBDyn and Chrono::Engine together represents a valid choice to simulate multibody systems coupled with particle dampers.

3. CO-SIMULATION METHOD

To achieve co-simulation of the two solvers, a tight coupling scheme is established in this Section. In the implementation, a few details, including the communication layer and the initial settings, are discussed as well.

3.1. Tight coupling scheme

A tight coupling scheme, also called the iterative coupling scheme [32], or the implicit coupling scheme [29], using the Gauss-Seidel configuration [32], is designed for the co-simulation between two solvers, MBDyn and Chrono::Engine. For the interface between two solvers, an embedded function approach [44] is used, by which Chrono::Engine is embedded into the iterative process of MBDyn. At each iteration, MBDyn provides the coupling motion, and Chrono::Engine performs a whole integration step to produce the resulting forces and torques, that are sent back to MBDyn. The flowchart of the tight coupling scheme is presented in Fig. 3, which is summarized as (from t_n to t_{n+1})

- **Step 0**: MBDyn predicts the motion of the multibody system as $\mathbf{y}_{n+1}^{(0)}$ and $\dot{\mathbf{y}}_{n+1}^{(0)}$, using Eqs. (5) and (6);

- **Step 1**: MBDyn computes the motion of the container after iteration $l(l \in \mathbb{N})$ from $\mathbf{y}_{n+1}^{(l)}$, as $\tilde{\mathbf{q}}_{n+1}^{(l)}$ and $\dot{\tilde{\mathbf{q}}}_{n+1}^{(l)}$, and sends them to Chrono::Engine;

- **Step 2**: Chrono::Engine integrates Eq. (19) to produce the generalized force vector, as $\tilde{\mathbf{f}}_{n+1}^{(l+1)}$, which is the resultant of the forces and torques that each particle exerts on the container, and sends it to MBDyn;

- **Step 3**: MBDyn calculates the state vector $\mathbf{y}_{n+1}^{(l+1)}$ with the external force vector;

- **Step 4**: if the convergence condition $\|\tilde{\mathbf{f}}_{n+1}^{(l+1)} - \tilde{\mathbf{f}}_{n+1}^{(l)}\| \leq \tilde{\epsilon}_1$ ($\tilde{\epsilon}_1 > 0$ is a small quantity representing the maximum admissible error) is satisfied, or the maximum number of iterations is reached, the dynamics equation of subsystem 1 is computed in MBDyn with $\tilde{\mathbf{f}}_{n+1}^{(l+1)}$ until the solution converges; otherwise, Steps 1–3 are repeated.

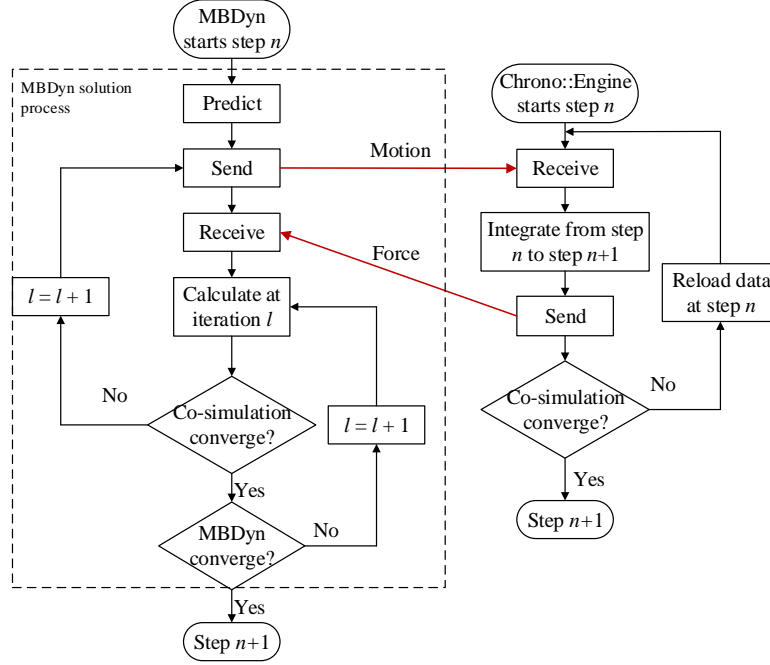[2]http://projectchrono.org/, last accessed June 2020.

Figure 3: Flowchart of the tight coupling scheme.

As one can see, the tight coupling scheme adopts a prediction-correction approach per step. The data communicated between the two solvers is corrected in each iteration, until the dynamics equations of the two subsystems are both satisfied in an approximate manner, either within the desired tolerance or a maximum number of iterations is reached. Of course, this coupling scheme can also be carried out without the iterative process, yielding the loose coupling scheme, as shown in Fig. 4, where the coupling forces produced from the predicted motion are employed for the calculation in MBDyn. In the following, this loose coupling scheme is used for comparison.

3.2. Implementation

3.2.1. Initial setting

In the process of adding particles to the damper in Chrono::Engine, the particles are settled in a simple cubic arrangement with clearances, whereas in most experiments the particles in the damper are usually assumed to be initially at rest under gravity. Therefore, the initial setting is needed to make the initial condition consistent.

Prior to the co-simulation, the particle damper, excited by a one-cycle sinusoidal perturbation, is simulated alone several times. In each simulation, when the kinetic energy of the particles vanishes to almost zero [34], the states are recorded as the initial positions for the next one, in which the height of the container is reduced while guaranteeing that it can hold all the particles. When the total height of the particles no longer reduces, the states are saved as the initial conditions for the co-simulation. The whole initial setting process thus corresponds to slightly shaking the particle damper with a decreasing height, so that the particles can be arranged with a reasonably small total height.
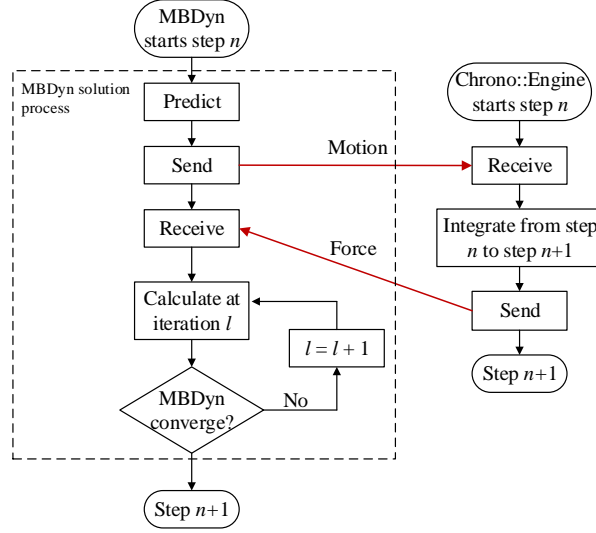
10

Figure 4: Flowchart of the loose coupling scheme.

3.2.2. Coupling variables

The two subsystems employ different global coordinate systems, as shown in Fig. 1, so a coordinate transformation is required during data exchange to keep the coupling variables consistent across the subsystems. The global coordinate system Ω_1 of subsystem 1 can be described in the global coordinate system Ω_2 of subsystem 2 by the position vector $\tilde{\mathbf{r}}_{1-2}$ and the orientation matrix $\tilde{\mathbf{R}}_{1-2}$. The transformation formula of the coupling variables, $\tilde{\mathbf{q}}$ and $\tilde{\mathbf{f}}$, in the two subsystems, can be written as:

$$
\begin{cases}
\tilde{\mathbf{q}}_{\mathbf{r},2} = \tilde{\mathbf{R}}_{1-2}\tilde{\mathbf{q}}_{\mathbf{r},1} + \tilde{\mathbf{r}}_{1-2}, \\
\tilde{\mathbf{q}}_{\mathbf{R},2} = \tilde{\mathbf{R}}_{1-2}\tilde{\mathbf{q}}_{\mathbf{R},1}, \\
\tilde{\mathbf{f}}_2 = \tilde{\mathbf{R}}_{1-2}\tilde{\mathbf{f}}_1,
\end{cases}
\tag{20}
$$

where $\tilde{\mathbf{q}}_{\mathbf{r}}$ and $\tilde{\mathbf{q}}_{\mathbf{R}}$ denote the position vector and the rotation matrix corresponding to the generalized coordinate $\tilde{\mathbf{q}}$, and the subscript $\tilde{i}$ ($\tilde{i} = 1, 2$) indicates the subsystem.

In the co-simulation, the transformation is executed before the coupling variables are sent to the corresponding solver, so the variables used in Eq. (18) are $\tilde{\mathbf{q}}_{\mathbf{r},2}$ and $\tilde{\mathbf{q}}_{\mathbf{R},2}$. Specifically, since Chrono::Engine employs quaternions [20] to represent rotations, $\tilde{\mathbf{q}}_{\mathbf{R},2}$ needs to be transformed into the quaternion $\tilde{\mathbf{q}}_{Q,2}$ after the coordinate transformation in Eq. (20). In MBDyn, on the contrary, although the incremental Cayley-Gibbs-Rodriguez (CGR) parameters [28] are used in the solution process, orientation is accumulated in form of rotation matrices, so no additional operations are required.

Another essential aspect of the coupling variables is how they enter the solution process in the corresponding solvers. In MBDyn, the input $\tilde{\mathbf{f}}_1$ is implemented as an external structural force element [28], directly applied to the nodes of the model. In Chrono::Engine, to prescribe the motion of the container using constraints in Eq. (18), the displacement $\tilde{\mathbf{q}}$ is obtained from

11

MBDyn, whereas the velocity $\dot{\tilde{\mathbf{q}}}$ is approximated using a forward finite difference scheme

$$\dot{\tilde{\mathbf{q}}}(t) = \frac{\tilde{\mathbf{q}}(t + \Delta t) - \tilde{\mathbf{q}}(t)}{\Delta t}, \tag{21}$$

where $\Delta t \ll h$ is a small time interval, and the function $\tilde{\mathbf{q}}(\cdot)$ is obtained by interpolation. For the displacement $\tilde{\mathbf{q}}_{\mathbf{r},2}$, linear interpolation during $[t_n, t_n + h]$ is employed to evaluate function $\tilde{\mathbf{q}}_{\mathbf{r},2}(\cdot)$, whereas for the quaternion $\tilde{\mathbf{q}}_{Q,2}$, the function $\tilde{\mathbf{q}}_{Q,2}(\cdot)$ is obtained using a first-order SLERP interpolation [45].

3.2.3. Communication tool

To practically couple the solvers, a stable and reliable two-way communication layer must be established to exchange data. Among the several possible architectural choices, standard sockets [46], based on the Transmission Control Protocol/Internet Protocol (TCP/IP) connection, are adopted in the proposed co-simulation scheme, owing to their reliability and stability. Before the co-simulation starts, the data-exchange channel is created in MBDyn, since it provides a simple scripting syntax and a full-featured multi-language library (libmbc) for establishing sockets through local (UNIX) / INET sockets [46] and to exchange the required data. For convenience, MBDyn is selected as the host. Considering that Chrono::Engine is distributed as a collection of C++ libraries, rather than a monolithic software like MBDyn, the C++ API of MBDyn's multi-body data interchange library is used to connect to the inter-process communication channel and exchange information through it.

4. STABILITY ANALYSIS

Dahlquist's test equation is commonly employed to study the stability of a monolithic simulation scheme [47], which can be interpreted as the mathematical representation of a linear single-mass oscillator [29]. Following that idea, Dahlquist's test equations for co-simulation methods can be understood as the equations governing the dynamical responses of a linear two-mass oscillator [29, 39], which is employed as the testing system to study the stability of a coupling scheme.

4.1. Two-mass oscillator

As in Fig. 5, the two-mass oscillator is decomposed into two subsystems. Subsystem 1 is simulated in MBDyn with the external force $\tilde{\lambda}$, calculated in subsystem 2. The simulation of subsystem 2 is based on Chrono::Engine with the rheonomic constraints that have been set up for the co-simulation. The dynamics equations of the two subsystems can be formulated as:

$$\dot{\mathbf{y}}_1 = \mathbf{F}_{11}\mathbf{y}_1 + \mathbf{F}_{12}\tilde{\lambda}, \tag{22}$$

and

$$\begin{cases} \dot{\mathbf{y}}_2 = \mathbf{F}_{21}\lambda + \mathbf{F}_{22}\mathbf{y}_2, \\ \mathbf{D}_{11}\mathbf{y}_2 = \tilde{x}_1, \end{cases} \tag{23}$$

with the coupling conditions:

$$\begin{cases} x_1 - \tilde{x}_1 = 0, \\ \lambda - \tilde{\lambda} = 0, \end{cases} \tag{24}$$

where $\mathbf{y}_i = [x_i, v_i]^{\mathrm{T}}$ ($i = 1, 2$, x_i and v_i denote the position and velocity) is the state vector of mass i; λ is the Lagrangian multiplier corresponding to the constraint equation in Eq. (23); $\tilde{\lambda}$ and $\tilde{x}_1$
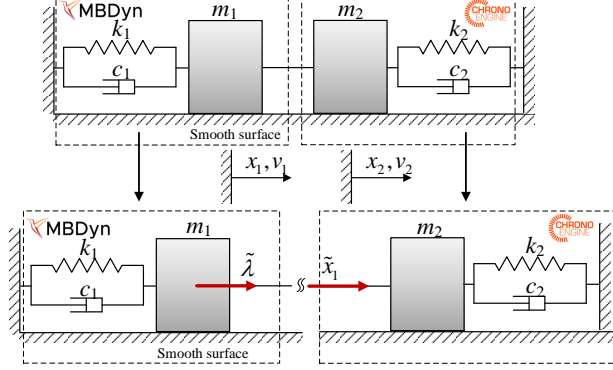
12

Figure 5: Decomposition of the two-mass oscillator.

are coupling variables; $\mathbf{D}_{11} = [1, 0]$ is the constant coefficient matrix and $\mathbf{D}_{11}\mathbf{y}_2 = \tilde{x}_1$ denotes the input position that is prescribed to subsystem 2 as a constraint; $\mathbf{F}_{ij}$ ($i = 1, 2, j = 1, 2$) depend on the system parameters as

$$
\mathbf{F}_{11} = \begin{bmatrix} 0 & 1 \\ -\dfrac{k_1}{m_1} & -\dfrac{c_1}{m_1} \end{bmatrix}, \quad
\mathbf{F}_{12} = \begin{bmatrix} 0 \\ \dfrac{1}{m_1} \end{bmatrix}, \quad
\mathbf{F}_{21} = \begin{bmatrix} 0 \\ -\dfrac{1}{m_2} \end{bmatrix}, \quad
\mathbf{F}_{22} = \begin{bmatrix} 0 & 1 \\ -\dfrac{k_2}{m_2} & -\dfrac{c_2}{m_2} \end{bmatrix},
$$

where m_i, k_i and c_i represent the mass, stiffness, and damping coefficient, as shown in Fig. 5.

4.2. Recurrence equations

The discrete equation of Eq. (22) at time t_{n+1} ($n \in \mathbb{N} \geq 2$) is

$$
\dot{\mathbf{y}}_{1,n+1} = \mathbf{F}_{11}\mathbf{y}_{1,n+1} + \mathbf{F}_{12}\tilde{\lambda}_{n+1}, \tag{25}
$$

which is solved using the implicit multi-step scheme, Eq. (2), in MBDyn. In Chrono::Engine, using the Euler semi-implicit scheme, Eq. (23) is discretized as

$$
\begin{cases}
\mathbf{y}_{2,n+1} = \mathbf{y}_{2,n} + h\mathbf{A}_0\mathbf{y}_{2,n+1} + h\mathbf{A}_1\mathbf{F}_{22}\mathbf{y}_{2,n} + h\mathbf{A}_1\mathbf{F}_{21}\lambda_{n+1}, \\
\dfrac{1}{h}(\mathbf{D}_{11}\mathbf{y}_{2,n} - \tilde{x}_{1,n}) + \left(\mathbf{D}_{12}\mathbf{y}_{2,n+1} - \dfrac{\tilde{x}_{1,n+1} - \tilde{x}_{1,n}}{h}\right) = 0,
\end{cases} \tag{26}
$$

where

$$
\mathbf{A}_0 = \begin{bmatrix} 0 & 1 \\ 0 & 0 \end{bmatrix}, \quad
\mathbf{A}_1 = \begin{bmatrix} 0 & 0 \\ 0 & 1 \end{bmatrix}, \quad
\mathbf{D}_{12} = \begin{bmatrix} 0 \\ 1 \end{bmatrix}^{\mathrm{T}}.
$$

Using the tight coupling scheme with the iterative process, the coupling condition (24) is approximately satisfied within the admissible error $\tilde{\epsilon}_1$, so its recurrence equations can be obtained from Eqs. (25) and (26), as

$$
\boldsymbol{\Lambda}_{1,\text{Tight}} \begin{bmatrix} \mathbf{y}_{1,n+1} \\ \mathbf{y}_{2,n+1} \\ \lambda_{n+1} \end{bmatrix} = \boldsymbol{\Lambda}_{2,\text{Tight}} \begin{bmatrix} \mathbf{y}_{1,n} \\ \mathbf{y}_{2,n} \\ \lambda_k \end{bmatrix} + \boldsymbol{\Lambda}_{3,\text{Tight}} \begin{bmatrix} \mathbf{y}_{1,n-1} \\ \mathbf{y}_{2,n-1} \\ \lambda_{n-1} \end{bmatrix}, \tag{27}
$$

13

with

$$\mathbf{\Lambda}_{1,\text{Tight}} = \begin{bmatrix} \mathbf{I} - hb_0\mathbf{F}_{11} & \mathbf{O} & -hb_0\mathbf{F}_{12} \\ \mathbf{O} & \mathbf{I} - h\mathbf{A}_0 & -h\mathbf{A}_1\mathbf{F}_{21} \\ -\dfrac{1}{h}\mathbf{D}_{11} & \mathbf{D}_{12} & \mathbf{O} \end{bmatrix},$$

$$\mathbf{\Lambda}_{2,\text{Tight}} = \begin{bmatrix} a_1\mathbf{I} + hb_1\mathbf{F}_{11} & \mathbf{O} & hb_1\mathbf{F}_{12} \\ \mathbf{O} & \mathbf{I} + h\mathbf{A}_1\mathbf{F}_{22} & \mathbf{O} \\ \mathbf{O} & -\dfrac{1}{h}\mathbf{D}_{11} & \mathbf{O} \end{bmatrix}, \tag{28}$$

$$\mathbf{\Lambda}_{3,\text{Tight}} = \begin{bmatrix} a_2\mathbf{I} + hb_2\mathbf{F}_{11} & \mathbf{O} & hb_2\mathbf{F}_{12} \\ \mathbf{O} & \mathbf{O} & \mathbf{O} \\ \mathbf{O} & \mathbf{O} & \mathbf{O} \end{bmatrix},$$

328 where $\mathbf{I}$ is the identity matrix, $\mathbf{O}$ is the zero matrix, and a_i ($i = 1, 2$) and b_i ($i = 0, 1, 2$) are the
329 coefficients defined in Eq. (3). Following the calculation steps of the loose coupling scheme , the
330 recurrence equations are derived as

$$\mathbf{\Lambda}_{1,\text{Loose}} \begin{bmatrix} \mathbf{y}_{1,n+1} \\ \mathbf{y}_{2,n+1} \\ \lambda_{n+1} \end{bmatrix} = \mathbf{\Lambda}_{2,\text{Loose}} \begin{bmatrix} \mathbf{y}_{1,n} \\ \mathbf{y}_{2,n} \\ \lambda_n \end{bmatrix} + \mathbf{\Lambda}_{3,\text{Loose}} \begin{bmatrix} \mathbf{y}_{1,n-1} \\ \mathbf{y}_{2,n-1} \\ \lambda_{n-1} \end{bmatrix}, \tag{29}$$

331 with

$$\mathbf{\Lambda}_{1,\text{Loose}} = \begin{bmatrix} \mathbf{I} - hb_0\mathbf{F}_{11} & \mathbf{O} & -hb_0\mathbf{F}_{12} \\ \mathbf{O} & \mathbf{I} - h\mathbf{A}_0 & -h\mathbf{A}_1\mathbf{F}_{21} \\ \mathbf{O} & \mathbf{D}_{12} & \mathbf{O} \end{bmatrix},$$

$$\mathbf{\Lambda}_{2,\text{Loose}} = \begin{bmatrix} a_1\mathbf{I} + hb_1\mathbf{F}_{11} & \mathbf{O} & hb_1\mathbf{F}_{12} \\ \mathbf{O} & \mathbf{I} + h\mathbf{A}_1\mathbf{F}_{22} & \mathbf{O} \\ \dfrac{1}{h}\mathbf{D}_{11}\left[(8b_0 + b_1)h\mathbf{F}_{11} + (a_1 - 12b_0)\mathbf{I}\right] & -\dfrac{1}{h}\mathbf{D}_{11} & (8b_0 + b_1)\mathbf{D}_{11}\mathbf{F}_{12} \end{bmatrix}, \tag{30}$$

$$\mathbf{\Lambda}_{3,\text{Loose}} = \begin{bmatrix} a_2\mathbf{I} + hb_2\mathbf{F}_{11} & \mathbf{O} & hb_2\mathbf{F}_{12} \\ \mathbf{O} & \mathbf{O} & \mathbf{O} \\ \dfrac{1}{h}\mathbf{D}_{11}\left[(5b_0 + b_2)h\mathbf{F}_{11} + (a_2 + 12b_0)\mathbf{I}\right] & \mathbf{O} & (5b_0 + b_2)\mathbf{D}_{11}\mathbf{F}_{12} \end{bmatrix}.$$

332 To facilitate the analysis, Eqs. (27) and (29) are uniformly rewritten as:

$$\mathbf{z}_{n+1} = \mathbf{\Lambda}\mathbf{z}_n, \tag{31}$$

333 with $\mathbf{z}_n = \begin{bmatrix} \mathbf{y}_{1,n}^{\text{T}} & \mathbf{y}_{2,n}^{\text{T}} & \lambda_{1,n}^{\text{T}} & \mathbf{y}_{1,n-1}^{\text{T}} & \mathbf{y}_{2,n-1}^{\text{T}} & \lambda_{1,n-1}^{\text{T}} \end{bmatrix}^{\text{T}}$ ($n \geq 2$), and

$$\mathbf{\Lambda} = \begin{bmatrix} \mathbf{\Lambda}_1^{-1}\mathbf{\Lambda}_2 & \mathbf{\Lambda}_1^{-1}\mathbf{\Lambda}_3 \\ \mathbf{I} & \mathbf{O} \end{bmatrix}. \tag{32}$$

4.3. Stability analysis

335 When the parameters in Eqs. (22)−(23) satisfy $m_1, m_2, k_1, k_2, c_1, c_2 > 0$, the two-mass oscillator
336 system is asymptotically stable. Under this condition, applying the coupling scheme to the equa-
337 tions of motion in Eqs. (22)−(23) yields a set of recurrence equations, as in Eqs. (27) and (29).
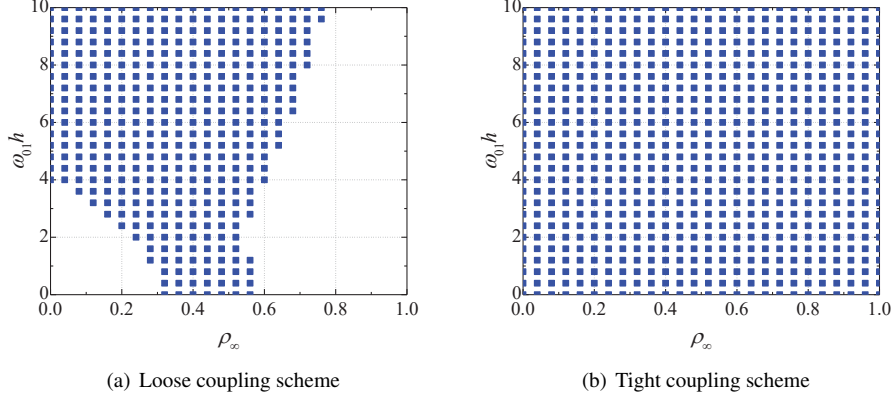
(a) Loose coupling scheme

(b) Tight coupling scheme

Figure 6: Stability plots with $\xi_1 = 0.0$, $r_m = 1.0$, $r_k = 0.0$ and $r_c = 0.0$ of different coupling schemes.

The coupling scheme is called stable when the recurrence equations give stable numerical so-
lutions [29], which can be determined considering the spectral radius of the coefficient matrix
$\mathbf{\Lambda}$ in Eq. (31), defined as $\tilde{\rho} = \max\{|\tilde{s}_i|\}$ ($i = 1, 2, \ldots, 10$), where $\tilde{s}_i$ are the eigenvalues of $\mathbf{\Lambda}$.
When $\tilde{\rho} \leq 1$, which is relaxed as $\tilde{\rho} \leq (1 + \tilde{\epsilon}_2)$ ($\tilde{\epsilon}_2$ is a small quantity, set as 10^{-6}) in the anal-
ysis due to small numerical errors in computing the eigenvalues, the scheme is stable, since the
numerical solutions remain bounded and do not diverge over time; otherwise, the scheme is un-
stable [29, 39]. In this way, the effect of the parameters of the sub-integrator, that is ρ_∞ of the
implicit multi-step scheme of Eq. (2), as well as the system parameters, that is m_i, k_i, c_i ($i = 1, 2$),
on the stability of the coupling scheme is discussed in this section.

In the analysis, the system parameters are expressed as $k_i = m_i\omega_{0i}^2$ N/m, $c_i = 2m_i\omega_{0i}\xi_i$ N · s/m,
where ω_{0i} and ξ_i are the natural frequency and the damping ratio of subsystem i. Besides, some
ratios reflecting the relationship between the parameters of the two subsystems are defined, as

$$r_m = \frac{m_2}{m_1}, \quad r_k = \frac{\omega_{02}}{\omega_{01}}, \quad r_c = \frac{\xi_2}{\xi_1}, \tag{33}$$

and $m_1 = 1$ kg is assumed.

The case of a conservative system, with $\xi_1 = 0$ (no structural damping), $r_m = 1.0$, $r_k = 0.0$
(i.e. $k_2 = 0$), $r_c = 0.0$ (i.e. $c_2 = 0$) is addressed first. The stability plots of the tight and loose
coupling schemes in the region $\rho_\infty \in [0, 1]$ and $\omega_{01}h \in [0, 10]$ are shown in Fig. 6, where the
blue squares indicate that the stability condition $\tilde{\rho} \leq (1 + \tilde{\epsilon}_2)$ is met. As expected, the tight
coupling scheme possesses a stability region greater than that of the loose one, because the
coupling conditions of Eq. (24) cannot be satisfied without iterations at each time step, leading
to instability of the loose coupling scheme in broad portion of the dissipation/frequency plane.
In addition, choosing the appropriate degree of algorithmic dissipation is also helpful to obtain
stable results, as shown in Fig. 6(a). When $\rho_\infty \in [0.32, 0.52]$, the loose coupling scheme is stable
regardless of $\omega_{01}h$, whereas when $\rho_\infty \notin [0.32, 0.52]$, it is stable only for large values of $\omega_{01}h$. As
a result, $\rho_\infty \in [0.32, 0.52]$ is recommended if the loose coupling scheme is employed, instead of
$\rho_\infty = 0.6$, a value suitable for the monolithic simulation [28].

With the same ξ_1, r_m, and r_c, the stability plots of the tight coupling scheme with different r_k
are shown in Fig. 7. An increase of r_k, namely a larger k_2 with respect to the same $\omega_{01}h$, shrinks

15

(a) $r_k = 0.1$

(b) $r_k = 0.3$

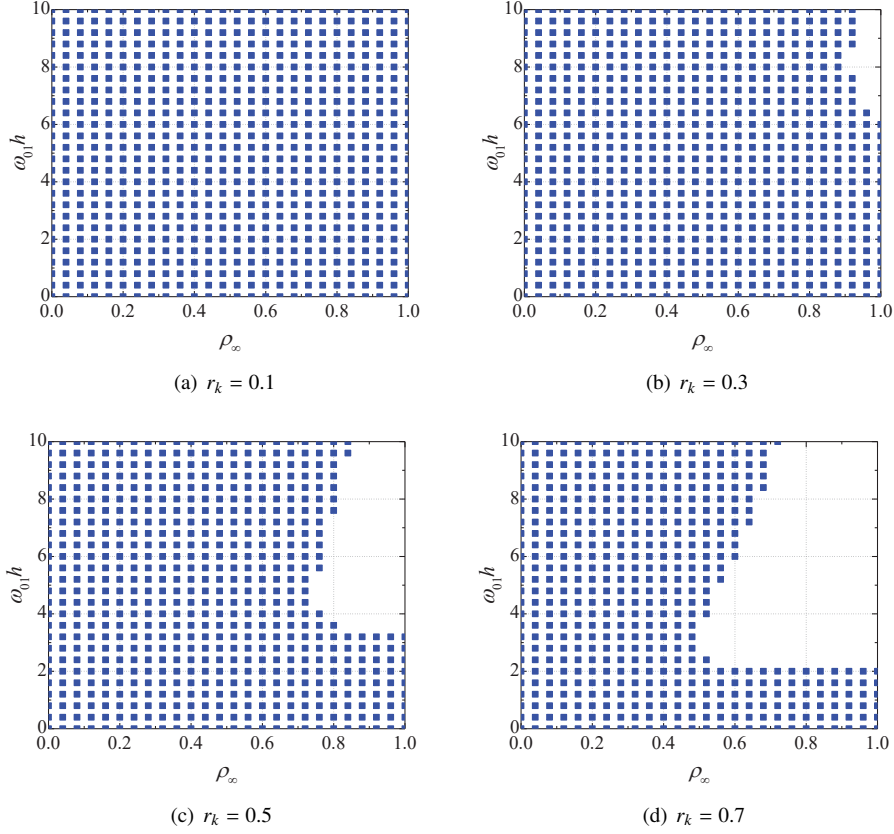(c) $r_k = 0.5$

(d) $r_k = 0.7$

Figure 7: Stability plots with $\xi_1 = 0.0$, $r_m = 1.0$, $r_c = 0.0$ and different r_k varying from $r_k = 0.1$ to $r_k = 0.7$ using the tight coupling scheme.

the stability region, because the errors caused by $\tilde{x}_1$ during the co-simulation can lead to greater changes in the acceleration with a larger k_2, resulting in algorithmic instability. For a specific r_k, the unstable cases occur with large $\omega_{01}h$, namely a larger time step or natural frequency. Besides, the proneness to instability can be mitigated by employing a smaller ρ_∞, to introduce stronger algorithmic dissipation in subsystem 1.

Figure 8 shows the stability plots of the tight coupling scheme with $\xi_1 = 0.6$, $r_k = 1.0$, $r_m = 1.0$, and different values of r_c. Trends similar to those highlighted above can be observed. A larger r_c, namely a larger c_2, can make the coupling scheme unstable in some cases, since the error caused by the coupling velocity $\tilde{v}_1$ is magnified during the co-simulation, resulting in algorithmic instability. However, the damping ratios improve the stability of the co-simulation. With $r_m = 1$, $r_k = 1$, $r_c = 1.0$ and different values of $\xi_1 = \xi_2$, the stability plots of the tight coupling scheme are presented in Fig. 9. It can be clearly seen that when $\xi_i = 0.0$, stability of the co-simulation is lost in most cases, whereas as ξ_i increases, the stability region grows.

The influence of the mass ratio r_m on stability is studied in a similar manner. Figure 10 presents the stability plots of the tight coupling scheme with $r_k = 0.7$, $r_c = 0.0$, $\xi_1 = 0.0$ and different values of r_m. It follows that as r_m decreases, the stability region grows, which can be
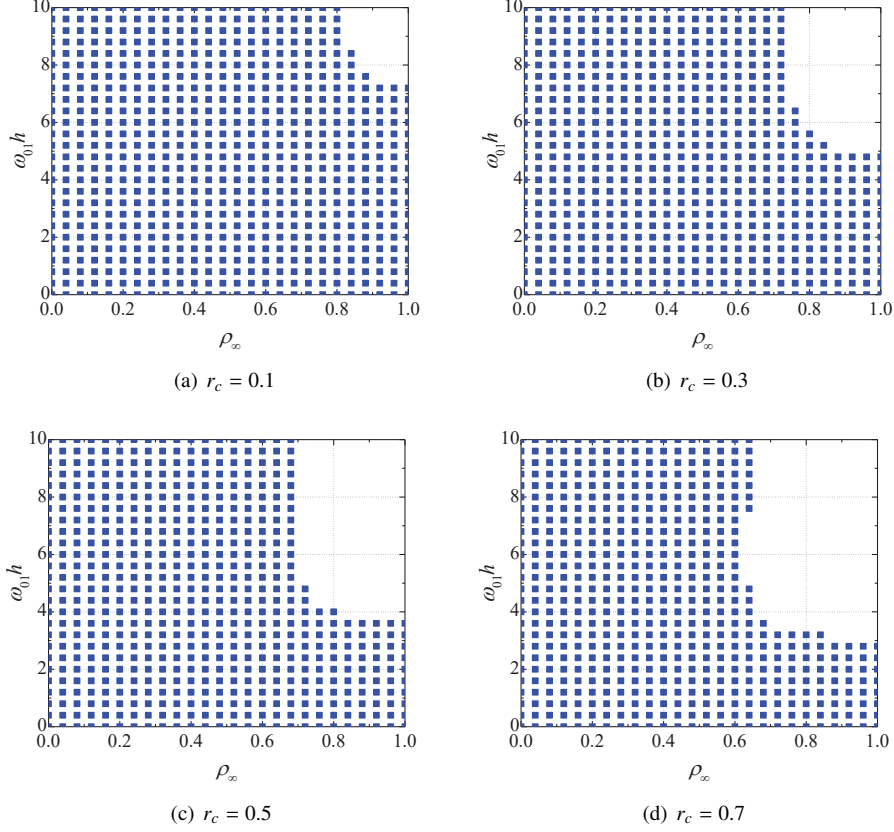
16

Figure 8: Stability plots with $\xi_1 = 0.6$, $r_m = 1.0$, $r_k = 1.0$ and different r_c varying from $r_c = 0.1$ to $r_c = 0.7$ using the tight coupling scheme.

interpreted with a reduction of the co-simulation error with the decrease of m_2. When $r_m = 0.0$, the co-simulation indeed becomes monolithic, based on the scheme of Eq. (2).

To verify the results of the stability analysis, a co-simulation is carried out, with the parameters $\rho_\infty = 0.60$, $\xi_i = 0.0$, $r_m = 1.0$, $r_k = 0.0$, $r_c = 0.0$, $h = 1 \times 10^{-4}$ s, $\omega_{01} = 10$, and the maximum admissible error $\tilde{\epsilon}_1 = 1 \times 10^{-6}$ for the tight coupling scheme. At the initial time, the oscillator is released at $x_1 = x_2 = 0.0$ m and $v_1 = v_2 = 1.0$ m/s. The time histories of v_1 obtained by the loose coupling scheme and the tight coupling scheme are presented in Fig. 11, which shows that for the loose coupling scheme, since in this case the spectral radius $\tilde{\rho}$ is larger than 1, as shown in Fig. 6(a), the results are divergent, while for the tight coupling scheme, oscillations with sensibly constant amplitude are observed because in this case $\tilde{\rho} < 1$, as shown in Fig. 6(b).

This set of parameters is employed to illustrate the convergence rate of the tight coupling scheme. With a fixed value $\omega_{01}^2 = 5000 \ s^{-2}$, the relative errors with different time steps h for simulations in the interval $[0, 0.1]$s are summarized in Table 1, where the relative error is
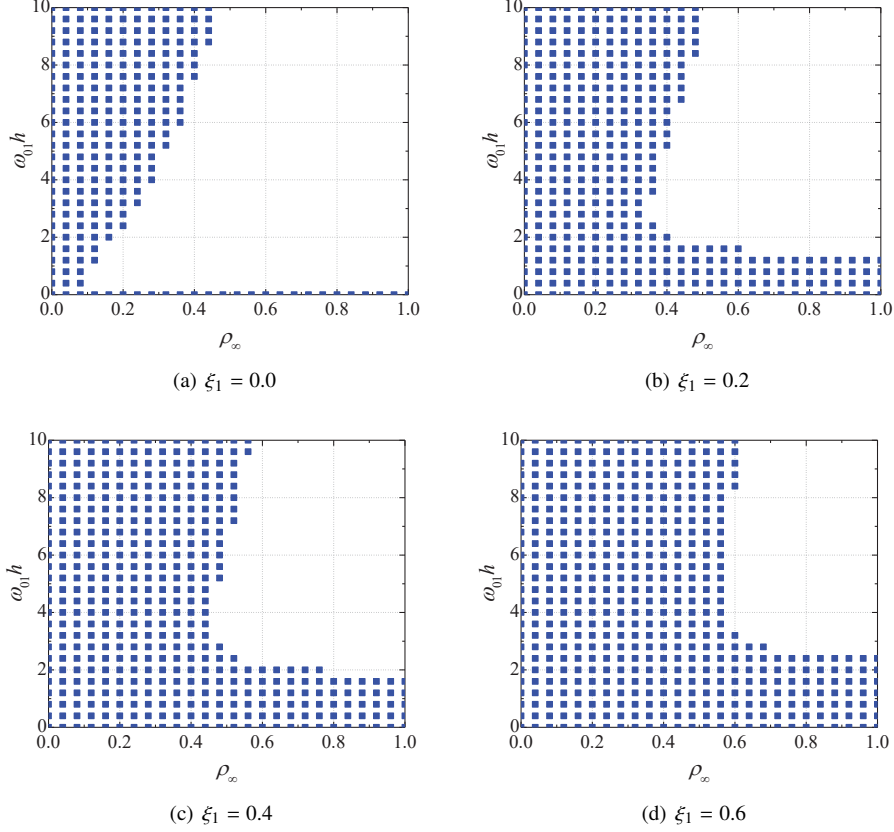
17

Figure 9: Stability plots with $r_m = 1.0$, $r_c = 1.0$, $r_k = 1.0$ and different ξ_1 varying from $\xi_1 = 0.0$ to $\xi_1 = 0.6$ using the tight coupling scheme.

evaluated as the L^1 norm, as [24]:

$$\|\text{error}\|_1 = \sum_{n=0}^{N} \left| x_{2,n} - x_2\left(t_n\right) \right| \bigg/ \sum_{n=0}^{N} \left| x_2\left(t_n\right) \right|, \tag{34}$$

where N is the number of steps, $x_{2,n}$ and $x_2(t_n)$ denote the co-simulation and analytical solution of x_2 at time t_n. From the results, the proposed coupling scheme can approximately achieve first-order accuracy. In this table, the number of required iterations, namely the number of times Chrono::Engine is called, the elapsed time and the CPU time during the co-simulation are also listed in the last two columns, to illustrate the computational cost of the tight coupling method. It follows that the computational cost mainly depends on the number of iterations, because as the time step size decreases, the computational cost of Chrono::Engine in each iteration, that is a whole integration from t_n to t_{n+1}, remains almost unchanged. When a smaller time step size is employed, each solver shows higher accuracy; thus, less iterations are required to achieve the admissible error $\tilde{\epsilon}_1$ and less time is required for each step. However, with a smaller step size, more steps are needed to reach the final time, resulting in higher overall computational cost, and
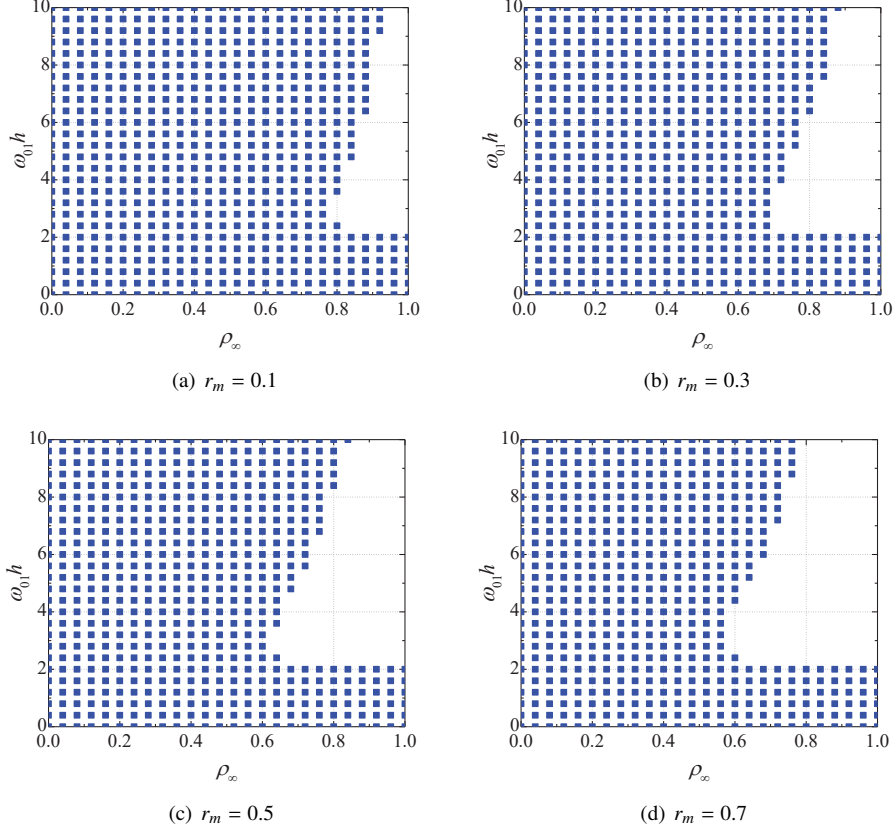
18

Figure 10: Stability plots with $\xi_1 = 0.0$, $r_c = 0.0$, $r_k = 0.7$ and different r_m varying from $r_m = 0.1$ to $r_m = 0.7$ using the tight coupling scheme.

more iterations are traded for the higher accuracy.

In conclusion, the stability of the proposed coupling scheme has been assessed using a simple two-mass oscillator. As expected, the tight coupling scheme shows a degree of algorithmic stability higher than that of the loose scheme. The algorithmic stability of the tight coupling scheme is affected by the parameters of the two subsystems, including the mass ratio, the natural frequency, and the damping ratio, as well as the asymptotic spectral radius ρ_∞ of the implicit integration method. Schemes with a smaller ρ_∞ can introduce higher algorithmic dissipation, which is helpful and convenient to avoid instability. The numerical results from co-simulation using the tight coupling scheme are consistent with the stability analysis; they also show that the proposed scheme approximately has first-order convergence rate.

5. RESULTS

In this section, two illustrative examples, the single-DoF primary system, used in the experiments reported in [26], and a cantilever beam modeled using finite volume elements [48], coupled with a particle damper, are simulated using the proposed co-simulation method discussed in Section 3,
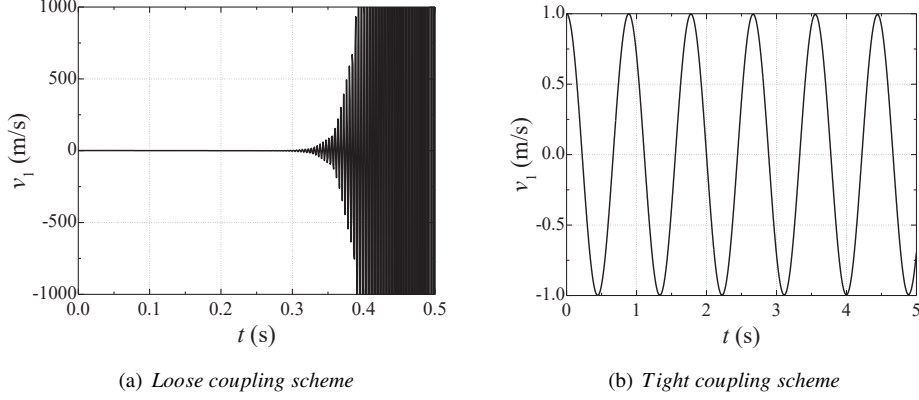
19

(a) *Loose coupling scheme*   (b) *Tight coupling scheme*

Figure 11: Time histories of v_1 using different coupling schemes with $\omega_{01}h = 0.001$.

Table 1: Relative error and time consumption of the tight coupling scheme during [0 0.1] s.

Time step size (s)	$\|\text{error}\|_1$	Number of iterations	Elapsed time (s)	CPU time (s)
1.0×10^{-3}	3.23×10^{-2}	1732	9.8	67.3
1.0×10^{-4}	3.29×10^{-3}	13957	82.0	644.2
1.0×10^{-5}	3.30×10^{-4}	87733	538.7	4192.0
1.0×10^{-6}	3.30×10^{-5}	367001	2569.8	20199.9

to assess its effectiveness. To improve the accuracy of the results, in Chrono::Engine millimeters and grams are used, whereas in MBDyn meters and kilograms are used. In the tight coupling scheme, the maximum admissible error $\tilde{\epsilon}_1$ for Chrono::Engine is set to 0.001, and a maximum of 20 iterations is used.

5.1. Single-DoF system with the particle damper

5.1.1. System description

The system is decoupled into two subsystems, as shown in Fig. 12. Subsystem 1, subjected to the external excitation x_{p1}, is simulated by MBDyn with the coupling variable $\tilde{F}$. Subsystem 2, the particle damper, is simulated using Chrono::Engine with the rheonomic constraint $x_{p2} = \tilde{x}_{p2}$. The system parameters of the experiment reported in [26], listed in Table 2, are used; m_r is the mass ratio of particles and container; about 200–250 particles are employed in the present simulation. At the initial time, the container of the particle damper is at rest on the ground. The sliding point of the primary system is excited by the sinusoidal signal $x_{p1} = X_{p1} \sin(2\pi f t)$.

5.1.2. Co-simulation results

After initialization, the two codes are connected with Unix sockets for data exchange. A fixed time step $h = 10^{-4}$ s is employed in the co-simulation. Results with $f = 12$ Hz and $m_r = 0.115$ are shown in Fig. 13, which presents the time histories of x_{p2} and v_{p2} at steady state resulting from three different methods: the monolithic simulation using the non-smooth method in Chrono::Engine, the loose coupling scheme (LCS), and the tight coupling scheme (TCS).
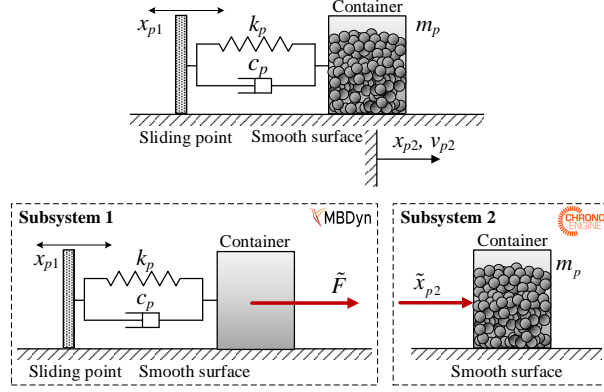
20

Figure 12: Decomposition of the system with a particle damper in the experiment reported in [26].
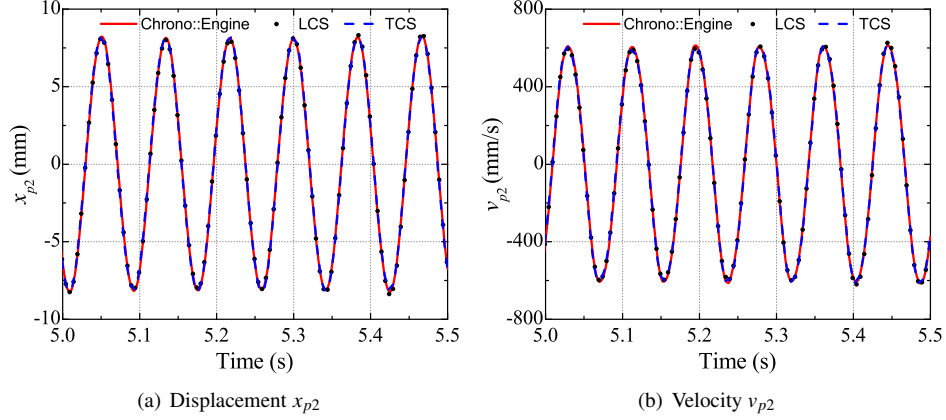

(a) Displacement x_{p2}

(b) Velocity v_{p2}

Figure 13: Time histories of displacement x_{p2} and velocity v_{p2} using different numerical methods.

The amplitudes of x_{p2} and v_{p2} are almost unchanged, since the energy absorbed by the particle and viscous dampers is approximately equal to that input by the excitation at steady state. The results obtained by the different methods overlap one another, illustrating the effectiveness of the coupling schemes.

Figure 14 shows the curves of the root mean square (rms) of x_{p2} versus the excitation frequency f with two mass ratios, $m_r = 0.092$ and $m_r = 0.115$. The co-simulation method (Cosim) using the tight coupling scheme gives a trend of the amplitude-frequency curve similar to that of the experimental one (Exp). For comparison, the frequency-amplitude curve for the case without particles is also plotted in Fig. 14 as the reference. Although the coupled system shows an amplitude slightly larger than that obtained without particles over the low frequency range, the particle damper effectively suppresses the resonance peak around the natural frequency of the main system. Results also show that the damper with $m_r = 0.115$ performs better than the damper with $m_r = 0.092$, as observed in the experiment [26].
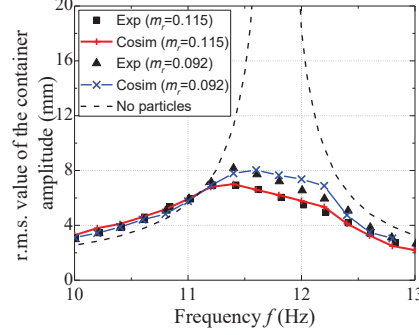
21

Figure 14: Curves of r.m.s. of the container amplitude versus frequency with different mass ratios m_r.

Table 2: Parameters of the system including particles in experiments [26].

	Parameters	Value	Parameters	Value
Subsystem 1	k_p (N/m)	1602.7	c_p (N · s/m)	0.116
	m_p (kg)	0.293		
Container	Length (mm)	58	Width (mm)	38
	Height (mm)	38		
Particles	Density (kg/m^3)	1190	Radius (m)	0.003
	m_r	0.092/0.115	Friction coefficient	0.52
Other	X_{p1} (m)	0.001	g (m/s^2)	9.8

5.2. Cantilever with the particle damper

5.2.1. System description

The cantilever beam coupled with a particle damper shown in Fig. 15(a) is studied in this Section. One end of the beam is constrained to the wall; a particle damper is attached at the other end. The beam is assumed to be uniform and made of isotropic material. Its parameters are listed in Table 3. The particle damper consists of lead particles encased in a cylindrical container, which is designed to have tunable clearance h_c between the particles and the ceiling. The parameters of the particle damper, including the material properties and the radius of the particles, are also shown in Table 3.

The system is decoupled in two subsystems, respectively simulated using MBDyn and Chrono::Engine, as shown in Fig. 15(a). The clamped end of the beam is established as the global coordinate for subsystem 1. The beam is modeled in MBDyn as a three-dimensional cantilever, meshed using 10 three-node beam elements, for a total of 21 nodes, without any structural damping. The container is modeled as a three-dimensional rigid body, whose rotary inertia with respect to the free end of the beam is assumed to be constant, as listed in Table 3. The external generalized force vector representing the reaction force and torque produced by the particles simulated in Chrono::Engine is applied to the container.

As a reference, the reduced model, which can be simulated using the monolithic method, is also used to reproduce the first bending mode, as shown in Fig. 15(b). It is composed of a two-
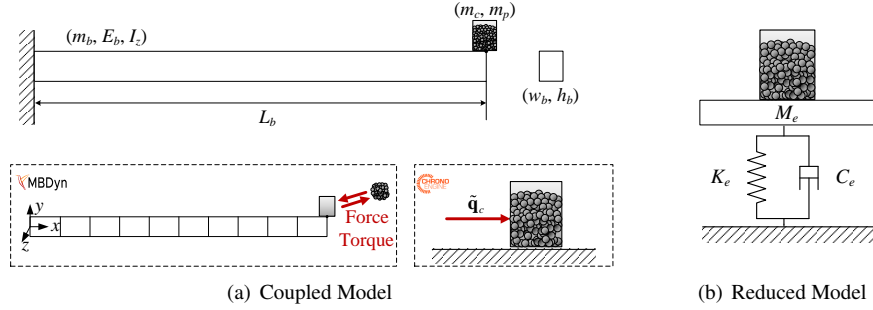
22

Figure 15: (a) Decomposition of the coupled model between a beam and a particle damper; (b) the reduced model.

Table 3: Parameters for the beam and the particle damper.

	Parameters	Value	Parameters	Value
Beam	Young's modulus E_b (GPa)	210	Poisson's ratio ν_b	0.33
	Destiny ρ_b (kg/m^3)	7845	Height h_b (m)	0.002
	Length L_b (m)	0.25	Width w_b (m)	0.03
	Mass m_b (g)	117.7		
Container	Mass m_c (g)	48.5	Inner radius r_c (m)	0.01
	J_{cx} (kg · mm^2)*	2.66	J_{cy} (kg · mm^2)*	4.85
	J_{cz} (kg · mm^2)*	2.66		
Particles	Radius r_p (m)	0.001	Destiny ρ_p (kg/m^3)	11344
	Friction coefficient μ_p	0.52	Total mass m_p (g)	7.0

* J_{cx}, J_{cy}, and J_{cz} are the components of the moment of inertia relative to the free
  end of the beam.

dimensional single-DoF primary structure, obtained from the cantilever. The rotary inertia of the particle damper's container is neglected, as in the model adopted in [7, 49, 50]. The equivalent mass M_e and stiffness K_e of the reduced model are obtained from [49, 50]:

$$\begin{cases} M_e = 0.24m_b + m_c + m_p, \\ K_e = \dfrac{3E_bI_{bz}}{L_b^3}, \end{cases} \tag{35}$$

where $I_{bz} = (w_bh_b^3)/12$ is the moment of inertia with respect to axis z. Since in the original model the structural damping of the beam is ignored, the equivalent damping C_e is also set as zero in the reduced model. The natural frequency of the reduced model is $\sqrt{K_e/M_e}/2\pi = 15.618$ Hz.

5.2.2. Co-simulation results

The modal analysis for the coupled model is performed in MBDyn using the method presented in [51]. In the analysis, the mass of the particles in the damper is added to that of the container. The resulting mode shapes of the first three bending modes in the $x - y$ plane are plotted
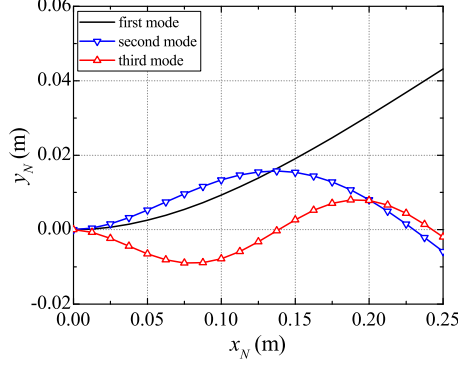
23

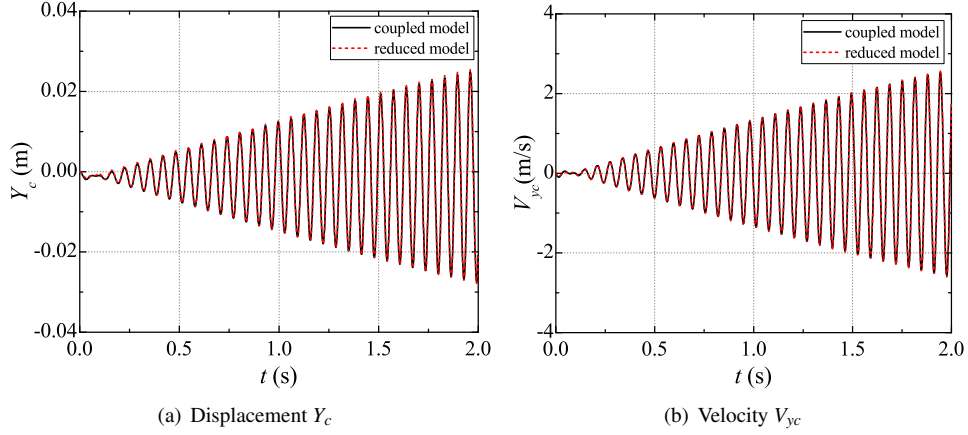Figure 16: First three calculated bending modes in the $x - y$ plane of the system with a lumped mass.

(a) Displacement Y_c

(b) Velocity V_{yc}

Figure 17: Time histories of the vertical displacement Y_c, and the vertical velocity V_{yc} using the coupled model and the reduced model with a lumped mass.

in Fig. 16. The corresponding natural frequencies are 15.619 Hz, 127.460 Hz and 381.082 Hz. The natural frequency of the reduced model is very close to that of the first bending mode.

With the particles modelled as additional lumped masses attached to the container, numerical simulations are carried out to compare the results of the two models excited by the external force $F_b = A_b \sin(2\pi f_b t)$ N. In the coupled analysis, the force is applied to the free end of the beam, whereas it is applied to the container in the reduced model. The time histories of the vertical displacement Y_c and velocity V_{yc} of the container with $h = 1 \times 10^{-4}$ s, $A_b = 0.25$ N and $f_b = 15.5$ Hz are plotted in Fig. 17. Since the excitation frequency is close to the first natural frequency, resonant response can be observed in both models. The numerical results of the two models overlap; this proves the equivalence of the reduced and coupled models in dealing with response close to the first normal vibration mode. Therefore, when the coupled model is subjected to an excitation close to the first natural frequency, the reduced model can be employed to check the performance of the coupling scheme.

The coupled model and the reduced model with the particle damper are then numerically sim-
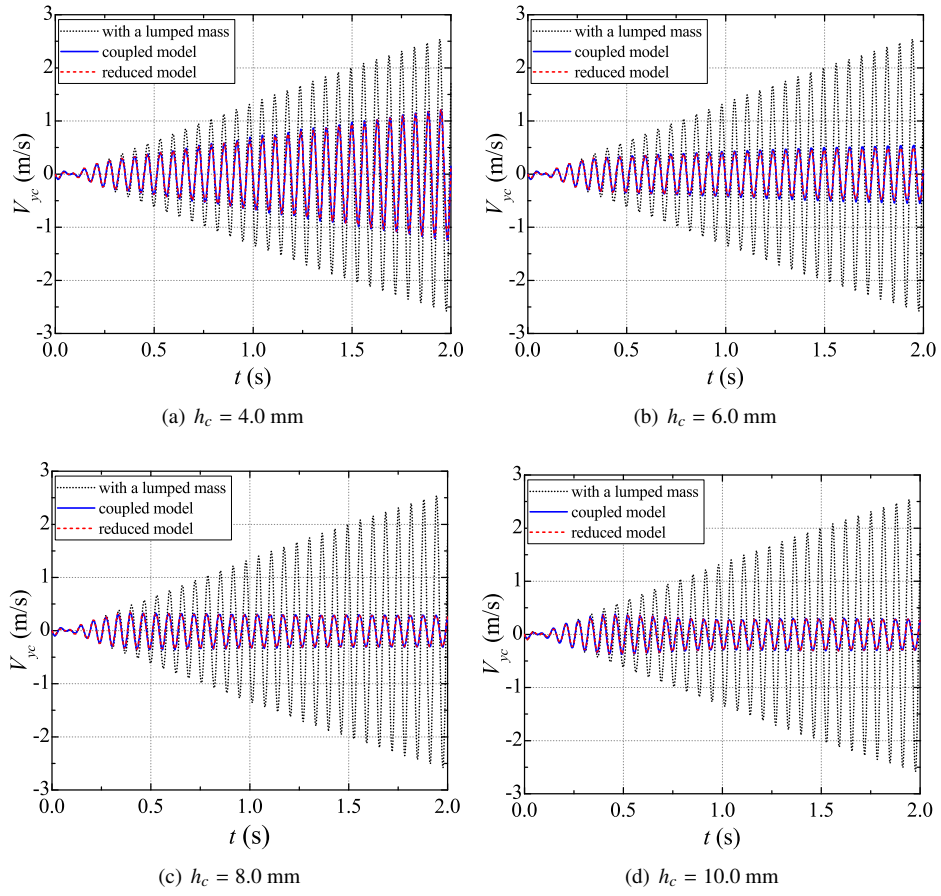
(a) $h_c = 4.0$ mm

(b) $h_c = 6.0$ mm

(c) $h_c = 8.0$ mm

(d) $h_c = 10.0$ mm

Figure 18: Time histories of the vertical velocity V_{yc} of the container obtained by the coupled model and the reduced model with different clearances h_c varying from $h_c = 4.0$ mm to $h_c = 10.0$ mm.
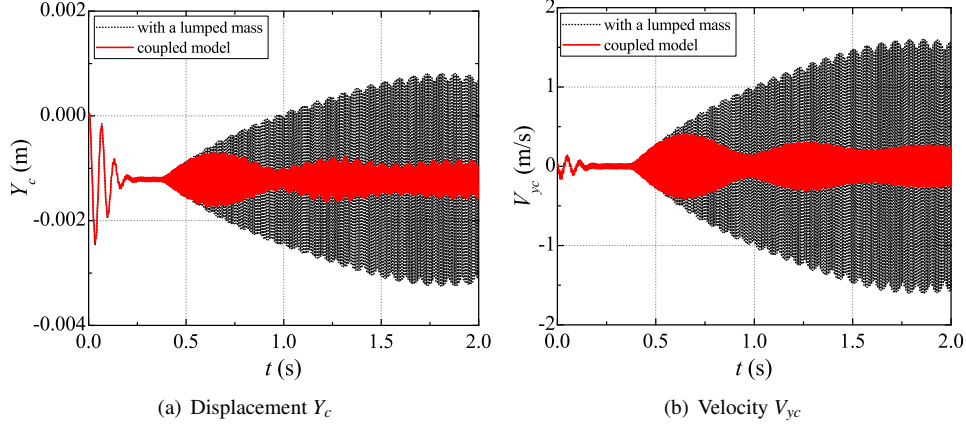
(a) Displacement Y_c (b) Velocity V_{yc}

Figure 19: Time histories of the vertical displacement Y_c, and velocity V_{yc} using the coupled model with a lumped mass or with particles under high-frequency excitation.

ulated using the tight coupling scheme and the monolithic method, respectively. The parameters are set as $h = 1 \times 10^{-4}$ s, $A_b = 0.25$ N, $f_b = 15.5$ Hz, and h_c changed from 4 mm to 10 mm. The time histories of the vertical velocities V_{yc} of the container are summarized in Fig. 18 with different clearances. The results of the coupled model using the tight coupling scheme are consistent with those of the reduced model using the monolithic method, which further validates the effectiveness of the coupling scheme. The results also show that the particle damper can effectively suppress the response at resonance; its damping effect is influenced by the clearance h_c. When h_c is less than 8 mm, the amplitude during [1.0, 2.0]s decreases along with the increase of h_c. When h_c is increased to values larger than 8 mm, the amplitude at steady state remains essentially constant. This phenomenon was also observed in the experiments [50], which indicates that the particle damper produces an increasingly significant damping effect as the clearance increases up to some threshold, after which, when the clearance is large enough, the damping effect remains constant. Therefore, the numerical results obtained in this work appear to be reasonable.

5.2.3. Vibration under high-frequency excitation

The damping effect of the particle damper under high-frequency excitation is then investigated using the tight coupling scheme. At higher frequencies, the high-order modes of the beam cannot be ignored; as such, the reduced model is not capable of reproducing the correct dynamic behavior. Figure 19 shows the result of the tight coupling scheme applied to the coupled beam/particle damper model. To suppress the oscillations resulting from the sudden application of gravity, artificial damping is applied to the beam during an initial transient, and gradually removed in the interval between 0 s and 0.4 s.

High-frequency excitation, with $A_b = 2.0$ N and $f_b = 127.0$ Hz, is then applied. With the parameters $\Delta t = 0.4$ s, $h_c = 4$ mm, and $h = 1 \times 10^{-5}$ s, the time histories of the displacement Y_c and the velocity V_{yc} of the container are plotted in Fig. 19. When the damping factor is reduced to a very small, constant value, resonance occurs when an equivalent lumped mass is added to the container instead of the particles, because now the excitation frequency is close to the second bending frequency of the beam. The results show that the particle damper can effectively

26

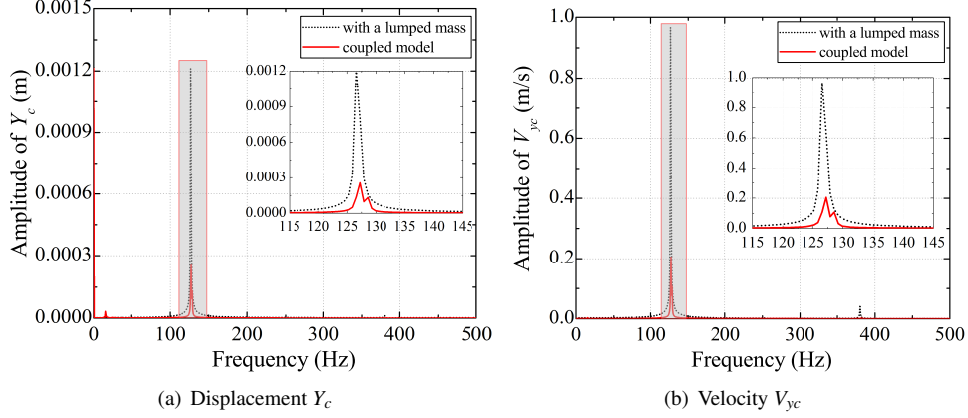(a) Displacement Y_c

(b) Velocity V_{yc}

Figure 20: Spectrum of the vertical displacement Y_c, and the vertical velocity V_{yc} by the coupled model and the reduced model with a lumped mass under high-frequency excitation.

suppress also the resonance of the high-order modes. The dynamic response in the $[0.5, 2.0]$ s interval in Fig. 19 is transformed into the frequency domain by the Fast Fourier Transform (FFT). The resulting amplitude-frequency curves of Y_c and $V_{y,c}$ are shown in Fig. 20. Owing to the effect of the particles, the amplitude of the coupled model is reduced compared with that with a lumped mass, consistent with Fig. 19.

5.2.4. Vibration under centrifugal loads

A test case in which the beam rotates about the y axis with constant angular velocity $\Omega = 2\pi \approx 6.28$ rad/s is also co-simulated, to show the ability to predict the damping produced by the particle damper under large full three-dimensional motion and centrifugal loads. The parameters of the system are listed in Table 3. The excitation is set as $A_b = 0.25$ N, $f_b = 15.5$ Hz. Co-simulation results for the particle damper with $h_c = 8$ mm are shown in Figs. 21 and 22, which present the trajectory of the container of the particle damper for $t \in [1.0, 1.5]$ s, and the time histories of the container's position components along the x, y, z axes. With the same angular velocity $\Omega = 2\pi \approx 6.28$ rad/s, results with the particle damper replaced by a rigid body of equivalent mass are also shown in Figs. 21 and 22, to illustrate the damping produced by the particle damper. It follows that under centrifugal loads the particle damper can still suppress vibrations in the direction of the rotation axis. Co-simulation results without centrifugal loads, namely $\Omega = 0.0$ rad/s, are also provided in Fig. 22. It can be seen that the damping effect of the particle damper is weakened. This can be justified by the perturbation the centrifugal loads introduce in the trajectory of the particles, as illustrated in the following. To further illustrate the influences of centrifugal loads, snapshots of particles in the local reference of the container are also presented in Fig. 23 for the non-rotating case, and in Fig. 24 for the rotating one. The snapshots show that in both cases, in the initial condition, the particles lie at the bottom of the container (a); close to the top of an oscillation ($t = 0.6$ s, as shown in Fig. 22(b)), they gather at the bottom of the container (b), whereas close to the bottom of an oscillation ($t = 1.6$ s, as shown in Fig. 22(b)), they gather at the top of the container (c). However, when subjected to centrifugal loads directed toward the right (outward direction, Fig. 24), the particles tend to pile up in that direction.
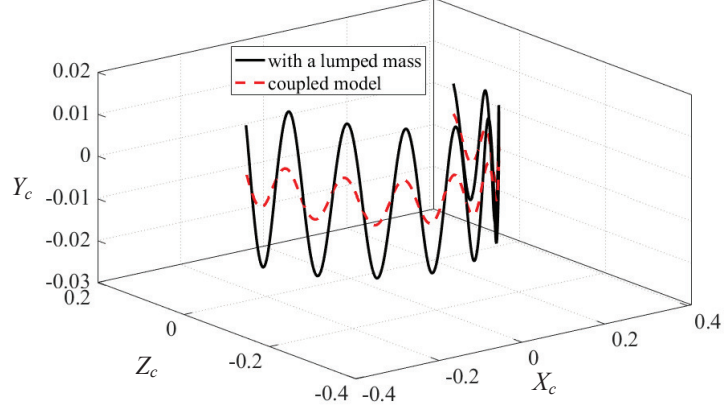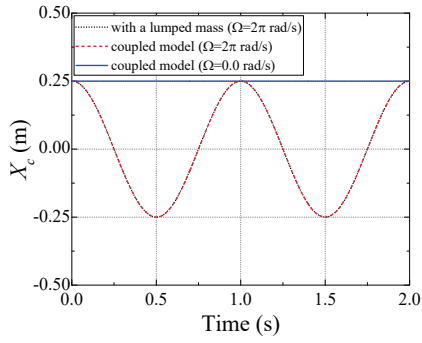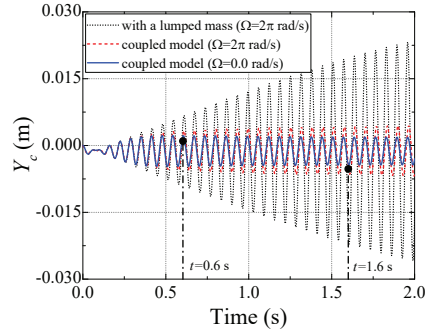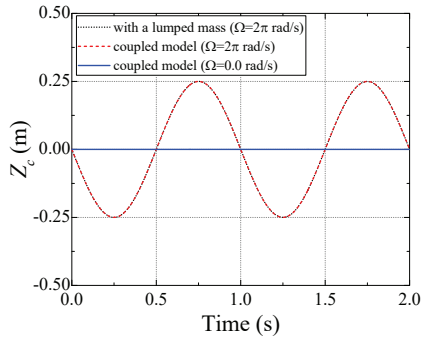
27

Figure 21: Trajectory of the container of the particle damper with constant angular velocity $\Omega = 2\pi \approx 6.28$ rad/s during $t \in [1.0, 1.5]$ s.

(a) Displacement X_c

(b) Displacement Y_c

(c) Displacement Z_c

Figure 22: Time histories of the container's position components along (a) x axis; (b) y axis; (c) z axis.

(a) $t = 0.0$ s (initial position) (b) $t = 0.6$ s (close to top of oscillation) (c) $t = 1.6$ s (close to bottom of oscillation)
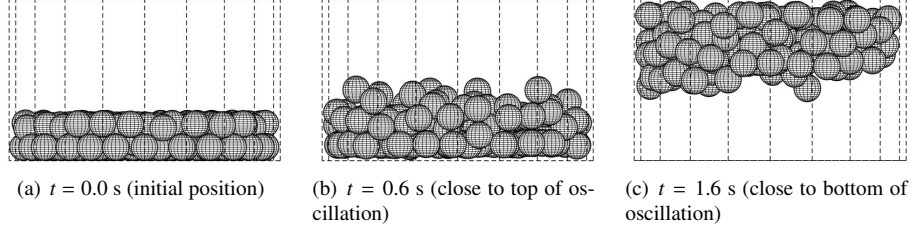
Figure 23: Snapshots of particles for $\Omega = 0.0$ rad/s: (a) $t = 0.0$ s (initial position); (b) $t = 0.6$ s (close to top of oscillation: particles gather at bottom of container); (c) $t = 1.6$ s (close to bottom of oscillation: particles gather at top of container)

(a) $t = 0.0$ s (initial position) (b) $t = 0.6$ s (close to top of oscillation) (c) $t = 1.6$ s (close to bottom of oscillation)
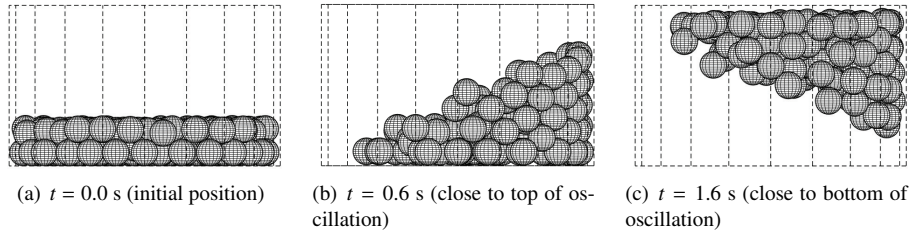
Figure 24: Snapshots of particles for $\Omega = 2.0\pi \approx 6.28$ rad/s: (a) $t = 0.0$ s (initial position); (b) $t = 0.6$ s (close to top of oscillation: particles gather at bottom of container); (c) $t = 1.6$ s (close to bottom of oscillation: particles gather at top of container)

Overall, when applied to the coupled model composed of a cantilever and a particle damper, the proposed tight coupling scheme shows satisfactory performance, which is checked using the reduced model and experimental results. The numerical results also illustrate that the particle damper is effective in damping resonance at different frequencies and under centrifugal loads.

6. CONCLUSIONS

A tight coupling scheme with iterations using two free general-purpose solvers, MBDyn and Chrono::Engine, is established to study the coupled dynamics of multibody systems with particle dampers. In the coupled configuration, Chrono::Engine is embedded into the iterative solution process of MBDyn to obtain algorithmically stable results, where only the non-smooth solver needs to be repeated in each step. The coupled system is decomposed in two subsystems using the force-displacement decomposition technique. The subsystem including the multibody system is simulated using the implicit A/L stable linear multi-step scheme implemented in MBDyn, whereas the subsystem including the particle damper is simulated using the non-smooth method based on the complementarity theory implemented in Chrono::Engine. The two solvers are connected by the coupling variables: the motion of the container produced by MBDyn is prescribed using rheonomic constraints in Chrono::Engine, and the forces and torques of the particles obtained from Chrono::Engine are applied to MBDyn as external forces. The data exchange is carried out at each iteration using a stable two-way communication protocol, established using sockets.

To assess the numerical stability of the proposed coupling scheme, Dahlquist's test equations for co-simulation methods, which can be regarded as the equation of a linear two-mass oscillator, is used. The corresponding recurrence scheme of the coupling approach is deduced. Using

29

the recurrence scheme, the algorithmic stability properties can be easily obtained by detecting whether the spectral radius of the recurrence scheme is greater than 1. It follows that the tight coupling scheme with iterations shows greatly improved algorithmic stability compared with the loose coupling scheme without iterations. Algorithmic stability is also influenced by the parameters of the subsystems and of the solvers. Excessive mass, natural frequency, or damping ratio in the subsystem built in Chrono::Engine, can lead to unstable co-simulation, whereas for subsystems with equal damping ratio, the stability region grows as the viscous damping increases. The algorithmic dissipation of the implicit integrator in MBDyn is beneficial to improve the stability of the coupling scheme. It provides a very convenient way to enhance the stability by just adopting a smaller asymptotic spectral radius ρ_∞ in the integrator. Based on this example, the results of numerical simulations also show that the proposed coupling scheme has first-order convergence rate, approximately.

Finally, the tight coupling scheme is applied to two illustrative models: a single-DoF primary system and a cantilever beam, both coupled to a particle damper. In the first example, the effectiveness of the proposed scheme is verified by comparing the results with those obtained from monolithic simulation and experiments. For the cantilever example, meshed using finite volume elements, the proposed scheme gives results consistent with the monolithic simulation applied to the reduced model, when the excitation frequency is close to the first natural frequency of the system. When higher natural frequencies are excited, or the beam rotates about a fixed axis, all aspects that cannot be included in the reduced model, the coupled model can still obtain stable and qualitatively sound solutions using the proposed scheme. The results show that the particle damper produces the desirable effect of appreciably suppressing the resonant response in various cases, such as at multiple bending natural frequencies, or under centrifugal loads.

Acknowledgements

Conflict of interest

The authors declare that they have no conflict of interest.

References

[1] L. Gagnon, M. Morandini, G. L. Ghiringhelli, A review of particle damping modeling and testing, Journal of Sound and Vibration (2019) 114865.

[2] Z. Lu, Z. Wang, S. F. Masri, X. Lu, Particle impact dampers: Past, present, and future, Structural Control and Health Monitoring 25 (2018) e2058.

[3] Z. Lu, B. Huang, Y. Zhou, Theoretical study and experimental validation on the energy dissipation mechanism of particle dampers, Structural Control and Health Monitoring 25 (2018) e2125.

[4] N. Ahmad, R. Ranganath, A. Ghosal, Modeling of the coupled dynamics of damping particles filled in the cells of a honeycomb sandwich plate and experimental validation, Journal of Vibration and Control 25 (2019) 1706–1719.

[5] C. Wong, M. Daniel, J. Rongong, Energy dissipation prediction of particle dampers, Journal of Sound and Vibration 319 (2009) 91–118.

[6] Z. Lu, S. F. Masri, X. Lu, Parametric studies of the performance of particle dampers under harmonic excitation, Structural Control and Health Monitoring 18 (2011) 79–98.

[7] K. Mao, M. Y. Wang, Z. Xu, T. Chen, Dem simulation of particle damping, Powder Technology 142 (2004) 154–165.

[8] Y.-C. Chung, Y.-R. Wu, Dynamic modeling of a gear transmission system containing damping particles using coupled multi-body dynamics and discrete element method, Nonlinear Dynamics 98 (2019) 129–149.

[9] P. A. Cundall, O. D. Strack, A discrete numerical model for granular assemblies, geotechnique 29 (1979) 47–65.

[10] M. Machado, P. Moreira, P. Flores, H. M. Lankarani, Compliant contact force models in multibody dynamics: Evolution of the hertz contact theory, Mechanism and Machine Theory 53 (2012) 99–121.

[11] X. Zheng, F. Zhang, Q. Wang, Modeling and simulation of planar multibody systems with revolute clearance joints considering stiction based on an lcp method, Mechanism and Machine Theory 130 (2018) 184–202.

[12] R. Zhang, Z. Zhao, X. Zheng, Q. Wang, Insight into the drift motion of a bouncing asymmetric dimer, Journal of Computational and Nonlinear Dynamics 14 (2019).

[13] J. J. Moreau, Unilateral contact and dry friction in finite freedom dynamics, in: Nonsmooth mechanics and Applications, Springer, 1988, pp. 1–82.

[14] M. Jean, The non-smooth contact dynamics method, Computer Methods in Applied Mechanics and Engineering 177 (1999) 235–257.

[15] F. Pfeiffer, M. Foerg, H. Ulbrich, Numerical aspects of non-smooth multibody dynamics, Computer Methods in Applied Mechanics and Engineering 195 (2006) 6891–6908.

[16] D. Melanz, L. Fang, P. Jayakumar, D. Negrut, A comparison of numerical methods for solving multibody dynamics problems with frictional contact modeled via differential variational inequalities, Computer Methods in Applied Mechanics and Engineering 320 (2017) 668–693.

[17] P. Flores, R. Leine, C. Glocker, Application of the nonsmooth dynamics approach to model and analysis of the contact-impact events in cam-follower systems, Nonlinear Dynamics 69 (2012) 2117–2133.

[18] P. Flores, R. Leine, C. Glocker, Modeling and analysis of planar rigid multibody systems with translational clearance joints based on the non-smooth dynamics approach, Multibody System Dynamics 23 (2010) 165–190.

[19] A. Tasora, M. Anitescu, A convex complementarity approach for simulating large granular flows, Journal of Computational and Nonlinear Dynamics 5 (2010).

[20] A. Tasora, M. Anitescu, A matrix-free cone complementarity approach for solving large-scale, nonsmooth, rigid body dynamics, Computer Methods in Applied Mechanics and Engineering 200 (2011) 439–453.

[21] A. Tasora, S. Benatti, D. Mangoni, R. Garziera, A geometrically exact isogeometric beam for large displacements and contacts, Computer Methods in Applied Mechanics and Engineering 358 (2020) 112635.

[22] Q. Chen, V. Acary, G. Virlez, O. Brüls, A nonsmooth generalized-α scheme for flexible multibody systems with unilateral constraints, International Journal for Numerical Methods in Engineering 96 (2013) 487–511.

[23] S. Rezaei, T. Schindler, Mixed timestepping schemes for nonsmooth mechanics with high frequency damping, arXiv preprint arXiv:1505.07666 (2015).

[24] R. Zhang, Y. Yu, Q. Wang, Q. Wang, An improved implicit method for mechanical systems with set-valued friction, Multibody System Dynamics 48 (2020) 211–238.

[25] H. Zhang, Y. Xing, A framework of time integration methods for nonsmooth systems with unilateral constraints, Applied Mathematics and Computation 363 (2019) 124590.

[26] M. Saeki, Impact damping with granular materials in a horizontally vibrating system, Journal of Sound and Vibration 251 (2002) 153–161.

[27] Z. Lu, X. Lu, H. Jiang, S. F. Masri, Discrete element method simulation and experimental validation of particle damper system, Engineering Computations (2014).

[28] P. Masarati, M. Morandini, P. Mantegazza, An efficient formulation for general-purpose multibody/multiphysics analysis, Journal of Computational and Nonlinear Dynamics 9 (2014).

[29] B. Schweizer, P. Li, D. Lu, Explicit and implicit cosimulation methods: stability and convergence analysis for different solver coupling approaches, Journal of Computational and Nonlinear Dynamics 10 (2015).

[30] G. Bulian, J. L. Cercos-Pita, Co-simulation of ship motions and sloshing in tanks, Ocean Engineering 152 (2018) 353–376.

[31] A. Peiret, F. González, J. Kövecses, M. Teichmann, Multibody system dynamics interface modelling for stable multirate co-simulation of multiphysics systems, Mechanism and Machine Theory 127 (2018) 52–72.

[32] I. Hafner, N. Popper, On the terminology and structuring of co-simulation methods, in: Proceedings of the 8th International Workshop on Equation-Based Object-Oriented Modeling Languages and Tools, pp. 67–76.

[33] S. Lommen, G. Lodewijks, D. L. Schott, Co-simulation framework of discrete element method and multibody dynamics models, Engineering Computations (2018).

[34] F. Fleissner, A. Lehnart, P. Eberhard, Dynamic simulation of sloshing fluid and granular cargo in transport vehicles, Vehicle System Dynamics 48 (2010) 3–15.

[35] A. Recuero, R. Serban, B. Peterson, H. Sugiyama, P. Jayakumar, D. Negrut, A high-fidelity approach for vehicle mobility simulation: Nonlinear finite element tires operating on granular material, Journal of Terramechanics 72 (2017) 39–54.

31

[36] R. Kübler, W. Schiehlen, Modular simulation in multibody system dynamics, Multibody System Dynamics 4 (2000) 107–127.

[37] R. Kübler, W. Schiehlen, Two methods of simulator coupling, Mathematical and Computer Modelling of Dynamical Systems 6 (2000) 93–113.

[38] B. Schweizer, D. Lu, Semi-implicit co-simulation approach for solver coupling, Archive of Applied Mechanics 84 (2014) 1739–1769.

[39] B. Schweizer, D. Lu, Stabilized index-2 co-simulation approach for solver coupling with algebraic constraints, Multibody System Dynamics 34 (2015) 129–161.

[40] A. Peiret, F. González, J. Kövecses, M. Teichmann, Co-simulation of multibody systems with contact using reduced interface models, Journal of Computational and Nonlinear Dynamics 15 (2020).

[41] J. Rahikainen, F. González, M. Á. Naya, J. Sopanen, A. Mikkola, On the cosimulation of multibody systems and hydraulic dynamics, Multibody System Dynamics (2020) 1–25.

[42] D. Negrut, R. Serban, A. Tasora, Posing multibody dynamics with friction and contact as a differential complementarity problem, Journal of Computational and Nonlinear Dynamics 13 (2018).

[43] M. Anitescu, A. Tasora, An iterative approach for cone complementarity problems for nonsmooth dynamics, Computational Optimization and Applications 47 (2010) 207–235.

[44] M. Trcka, M. Wetter, J. Hensen, Comparison of co-simulation approaches for building and HVAC/R system simulation, in: Proceedings of the International IBPSA Conference, Beijing, China.

[45] K. Shoemake, Animating rotation with quaternion curves, in: Proceedings of the 12th Annual Conference on Computer Graphics and Interactive Techniques, pp. 245–254.

[46] T. Solcia, P. Masarati, Efficient multirate simulation of complex multibody systems based on free software, in: ASME 2011 International Design Engineering Technical Conferences and Computers and Information in Engineering Conference, American Society of Mechanical Engineers Digital Collection, pp. 29–39.

[47] G. G. Dahlquist, A special stability problem for linear multistep methods, BIT Numerical Mathematics 3 (1963) 27–43.

[48] G. L. Ghiringhelli, P. Masarati, P. Mantegazza, Multibody implementation of finite volume C^0 beams, AIAA journal 38 (2000) 131–138.

[49] R. D. Friend, V. Kinra, Particle impact damping, Journal of Sound and Vibration 233 (2000) 93–118.

[50] M. Trigui, E. Foltete, M. Abbes, T. Fakhfakh, N. Bouhaddi, M. Haddar, An experimental study of a multi-particle impact damper, Proceedings of the Institution of Mechanical Engineers, Part C: Journal of Mechanical Engineering Science 223 (2009) 2029–2038.

[51] P. Masarati, Direct eigenanalysis of constrained system dynamics, Proceedings of the Institution of Mechanical Engineers, Part K: Journal of Multi-body Dynamics 223 (2009) 335–342.